UNIVERSITY OF CALIFORNIA
RIVERSIDE

The Semi-Direct Aerosol-Cloud Effects

A Dissertation submitted in partial satisfaction
of the requirements for the degree of

Doctor of Philosophy

in

Geological Sciences

by

Anahita Amiri Farahani

December 2018

Dissertation Committee:

Dr. Robert J. Allen, Chairperson
Dr. Richard A. Minnich
Dr. Roya Bahreini

The Dissertation of Anahita Amiri Farahani is approved:

_____

_____

_____

Committee Chairperson

University of California, Riverside

Acknowledgements

I would have never been able to finish my dissertation if I had not been lucky enough to have the constant support of a few individuals. First, I owe my deepest gratitude to my advisor, Professor Robert J. Allen. His time, encouragement, support, professional mentorship and critical eye have been invaluable, and crucial to my success in graduate school. This work would have not been possible without his inimitable expertise and generous patience.

I would also like to thank Professor Richard A. Minnich and Professor Roya Bahreini for agreeing to be on my committee and for reading this thesis.

I would like to thank the Zeno Karl Schindler Foundation for granting me a doctoral exchange scholarship which allowed my visit to ETH Zurich and also the whole Wolke-group for their warm hospitality during my visit.

Special thanks go to my parents Soudeh and Reza and my brother Kaveh for instilling within me an appreciation for education, and for providing me with constant support and encouragement. I am especially grateful for my husband Kaveh, without whom the world would be a very unenjoyable place. Thank you for the gift of your love and support over the past 14+ years. I thank my son, Aubteen for providing me with extra motivation and brightening during my research with his wonderful smile and contagious laugh.

The text of this dissertation, in part, is a reprint of the material from the following publication: Amiri-Farahani, A., Allen, R. J., Neubauer, D., and Lohmann, U.: 2017, Atmospheric Chemistry and Physics 17(10), 6305

To my son Aubteen

ABSTRACT OF THE DISSERTATION

The Semi-Direct Aerosol-Cloud Effects

by

Anahita Amiri Farahani

Doctor of Philosophy, Graduate Program in Geological Sciences
University of California, Riverside, December 2018
Dr. Robert J. Allen, Chairperson

This thesis is composed of two parts. In the first part we investigate the impact of Saharan dust on North Atlantic marine stratocumulus clouds (MSc) using Cloud-Aerosol Lidar and Infrared Pathfinder Satellite Observation (CALIPSO), Clouds and the Earth's Radiant Energy System (CERES), and European Centre for Medium-Range Weather Forecasts Interim Re-Analysis (ERA-Interim). To calculate the aerosol- cloud radiative effect, we use two different methods These two methods yield similar results that Saharan dust modifies MSc in a way that acts to cool the planet. There is a strong seasonal variation, with the aerosol-cloud radiative effect switching from significantly negative during the boreal summer to weakly positive during boreal winter. When most dust resides above the clouds during summer, aerosol-cloud microphysical effects that involve the co-location of aerosol and cloud, such as the second aerosol indirect effect, would likely be muted relative to the SDE. Moreover, the positive value of the aerosol-cloud radiative effect during winter, when most dust resides within MSc, indicates that the semi-direct effect is dominant— that is the only mechanism by a negative aerosol-cloud radiative effect can be obtained. We conclude that aerosol-cloud radiative effects associated with Saharan dust and North Atlantic MSc are dominated by the semi-direct effect.

In the second part of the thesis we investigate the semi-direct effect using multiple general circulation models driven by observationally constrained fine-mode aerosol forcing without dust and sea salt. We find a significant global annual mean decrease in low and mid-level clouds, and weaker decreases in high-level clouds, which leads to a positive semi-direct effect dominated by shortwave radiation. Our results suggest that model simulations lead to a negatively biased semi-direct effect, due to an aerosol atmospheric heating profile that is too vertically uniform.

Contents

List of Figures

List of Tables

Chapter 1

Introduction

1.1 The radiative forcing concept

Radiative forcing is the net change in the energy balance of the Earth system due to some imposed perturbation. The instantaneous RF refers to an instantaneous change in net (down minus up) radiative flux (shortwave plus longwave; in W m^{-2}) due to an imposed change. This forcing is usually defined in terms of flux changes at the top of the atmosphere (TOA) or at the climatological tropopause, with the latter being a better indicator of the global mean surface temperature response in cases when they differ. A radiative forcing (RF) is linked to a change in global annual mean surface temperature (ΔT) through the climate sensitivity parameter (λ): $\Delta T = (RF)\lambda$. The relationship between RF and ΔT is an expression of the energy balance of the climate system and a simple reminder that the steady state global mean climate response to a given forcing is determined both by the forcing and responses inherent in λ. Forcing is often presented as the value due to changes between two particular times, such as pre-industrial to present-day, when its time evolution provides a more plete picture. In the RF concept all surface and tropospheric conditions are kept fixed, the effective radiative forcing (ERF) concept is similar, but all physical variables are allowed to respond to perturbations except for those concerning the ocean and sea ice. The inclusion of these adjustments makes ERF a better indicator of the eventual temperature response. ERF and RF values are significantly different for anthropogenic

aerosols owing to their influence on clouds and snow cover (Boucher et al., 2013).

Changes in cloud cover and cloud microphysical properties are a source of uncertainty in the projection of future climate change due to RF. One of the main sources of uncertainty is the impact of aerosols (tiny particles suspended in the air) on the climate system. Aerosols are produced both naturally (sea salt) and by human activities, such as bustion of fossil fuels and biomass burning. Concentration of aerosols in the troposphere has increased over the last 150 years due to human activity. The impact of aerosols on the climate system is poorly understood, due to the plexity of their physical, chemical and optical properties, their variability in space and time, and their interaction with clouds.

1.2 Effects of aerosols on climate

Aerosols have several effects on climate. First, they interact directly with solar radiation either through scattering or absorption (the direct effect). Some aerosols cause a negative forcing like sulfate -0.4 (-0.6 to -0.2) W m^{-2} while others cause a positive forcing such as black carbon +0.4 (+0.05 to +0.8) W m^{-2}. The total direct aerosol RF as derived from models and observations is estimated to be -0.35 ± 0.5 W m^{-2} with a medium-low level of scientific understanding.

Second, they have indirect effects on climate by altering microphysical and radiative properties of clouds. Aerosols can act as cloud condensation nuclei. The microphysically induced effect on the cloud droplet number concentration and hence the cloud droplet size, with the liquid water content held fixed has been called the “first indirect effect” , “cloud albedo effect” , or the “Twomey effect”. The microphysically induced effect on the liquid water content, cloud height and lifetime of clouds has been called the “second indirect effect”, “the cloud lifetime effect”. The indirect effect is considered as a key uncertainty in RF of climate, and its range is between 0 and -2 W m^2 in the context of liquid water clouds.

Furthermore, aerosols that are highly absorbing of solar radiation, such as black carbon and dust, may reduce cloud cover and liquid water content by heating the cloud and environment within which the cloud forms. This is the original “semi-direct” effect (SDE) first described by

Hansen et al. (1997); because it is the result of direct interaction of aerosols with radiation but also influences climate indirectly by altering clouds. SDE is the mechanism by which absorption of shortwave radiation by tropospheric aerosols leads to heating of the troposphere that in turn changes the relative humidity and the stability of the troposphere and thereby influences cloud formation and lifetime (Boucher et al., 2013). The additional heat from aerosol absorption reduces the relative humidity of the layer thereby promoting the evaporation of clouds. The positive climate forcing results from the reduction of bright cloud exposing a darker surface underneath. Recent studies, however, suggest absorbing aerosols may result in the opposite response- increased cloud cover and surface cooling- under certain scenarios (e.g., Johnson et al., 2004; Allen and Sherwood, 2010a). When the absorbing aerosol resides above a low cloud deck the absorption of sunlight by the aerosols causes a reduction in cloud-top entrainment that leads to a thickening of the cloud deck (Wilcox, 2010; Johnson et al., 2004). Thicker clouds are, in general, brighter, thus yielding a negative RF. Thus, there may be multiple semi-direct effects that have opposing effects on cloud cover and surface temperature.

The SDE is poorly understood, and it is unclear how important it is in comparison to the direct and indirect effects. For the SDE, even the sign of radiative forcing is not well known at present (with a very low level of scientific understanding), but its magnitude is probably smaller than those of indirect effects. Available estimates suggest a range of -0.3 to +0.1 W m^{-2}; this large uncertainty is parable to that for aerosol indirect effects. This illustrates that the aerosols represent one of the largest uncertainties in our estimates of past and future changes in radiative forcing. Previous studies have described conditions under which absorbing aerosols (AAs) either increase or decrease cloud cover. The effect depends on several factors, including the altitude of the AAs relative to the cloud and cloud type (Koch and Del Genio, 2010). For AAs below the cloud level, the heating below cloud enhanced vertical motions and increased cloud cover and Liquid water path. Absorbing aerosols aloft generally stabilize the atmosphere beneath. Increased stability over stratocumulus strengthens the inversion, reduces cloud-top entrainment of overlying dry air and thereby enhances the underlying clouds(Koch and Del Genio, 2010). AAs above shallow cumulus in oceanic region might also strengthen the inversion

and promote transition to a stratocumulus regime with increased cloud cover. For AAs above low cumulus clouds over land, the enhanced stability can reduce convective cloud formation. As within cloud reduce cloud cover, due to reduced relative humidity (the traditionally defined semi-direct effect). For low-mid-altitude clouds, this leads to a positive semi-direct effect and for high clouds, this leads to a negative semi-direct effect.

In Chapter 2, I present the results of impact of dust on North Atlantic marine stratocumulus clouds and show the importance of semi-direct effects. In Chapter 3, I show that aerosol-cloud semi-direct effects enhance warming of the climate system. Finally, Chapter 4 summarizes the most important findings.

Chapter 2

Impact of Saharan dust on North Atlantic marine stratocumulus clouds: Importance of the semi-direct effect

Abstract

One component of aerosol-cloud interactions (ACI) involves dust and marine stratocumulus clouds (MSc). Few observational studies have focused on dust-MSc interactions, thus this effect remains poorly quantified. We use observations from multiple sensors in the NASA A-Train satellite constellation from 2004 to 2012 to obtain estimates of the aerosol-cloud radiative effect, including its uncertainty, for dust aerosol influencing Atlantic MSc off the coast of North Africa between 45°W and 15°E, and 0-35°N. To calculate the aerosol-cloud radiative effect, we use two methods following Quaas et al. (2008) (Method 1) and Chen et al. (2014) (Method 2). These two methods yield similar results of $-1.5\pm$ 1.4 and $-1.5\pm$ 1.6 Wm^{-2}, respectively, for the annual mean aerosol-cloud radiative effect. Thus, Saharan dust modifies MSc in a way that acts to cool the planet. There is a strong seasonal variation, with the aerosol-cloud radiative effect switching from significantly negative during the boreal summer to weakly positive during boreal winter. Method 1 (Method 2) yields -3.8 ±2.5 (-4.3 ± 4.1) during summer, and 1 ±2.9 (0.6 ± 1)

Wm^{-2} during winter. In Method 1, the aerosol-cloud radiative effect can be decomposed into two terms, one representing the first aerosol indirect effect and the second representing the combination of the second aerosol indirect effect and the semi-direct effect (i.e., changes in liquid water path and cloud fraction in response to changes in absorbing aerosols and local heating). The first aerosol indirect effect is relatively small, varying from -0.7 ± 0.6 in summer to 0.1 ± 0.5 Wm^{-2} in winter. The second term, however, dominates the overall radiative effect, varying from -3.2 ±2.5 in summer to 0.9 ± 2.9 Wm^{-2} during winter. Studies show that the semi-direct effect can result in a negative (i.e., absorbing aerosol lies above low clouds like MSc) or positive (i.e., absorbing aerosol lies within low clouds) aerosol-cloud radiative effect. The semi—permanent MSc are low and confined within the boundary layer. CALIPSO shows that 61.8% ±12.6% of Saharan dust resides above North Atlantic MSc during summer for our study area. This is consistent with a relatively weak first aerosol indirect effect, and also suggests the second aerosol indirect effect plus semi-direct effect (the second term in Method 1) is dominated by the semi-direct effect. In contrast, the percentage of Saharan dust above North Atlantic MSc in winter is 11.9% ±10.9% which is much lower than in summer. CALIPSO also shows that 88.3% ±8.5% of dust resides below 2.2 km the winter average of MSc top height. During summer, however, there are two peaks, with 35.6% ±13% below 1.9 km (summer average of MSc top height) and 44.4% ±9.2% between 2 and 4 km. Because the aerosol-cloud radiative effect is positive during winter, and is also dominated by the second term, this again supports the importance of the semi-direct effect. We conclude that Saharan dust-MSc interactions off the coast of north Africa are likely dominated by the semi-direct effect.

2.1 Introduction

To reduce uncertainty in climate sensitivity and future global warming estimates, it is necessary to quantify the radiative forcing of aerosols. However there is a large uncertainty in aerosol radiative forcing, and much of this uncertainty is related to the magnitude of indirect aerosol effects on clouds of -0.45 Wm^{-2} with an uncertainty range of -1.2 to 0 Wm^{-2}

(Boucher et al., 2013). Aerosols also impact clouds through "rapid adjustments" associated with aerosol-radiation interactions, otherwise known as semi-direct effects (SDE). Available estimates suggest a relatively large SDE uncertainty of -0.3 to $+0.1$ Wm^{-2} (Boucher et al., 2013). The growing interest in the impact of aerosols on climate has stimulated the development of better physically based parameterizations of aerosols and aerosol-cloud interactions (ACI) in climate models. Nevertheless, the lack of understanding of external forcing on clouds remains one of the largest uncertainties in climate modeling and climate change projections.

One aspect of ACI is the possible influence of dust on marine stratocumulus (MSc) clouds. North Africa is the world's largest dust source (Goudie and Middleton, 2001). Dust emissions from this region occur from both the hyper-arid Sahara and the semi-arid Sahel. Africa is responsible for approximately half of the global emissions (Huneeus et al., 2011) with several hundred teragrams of dust being transported across the Atlantic towards the Americas throughout the year (Kaufman et al., 2005). This has consequences for air quality downwind (Prospero, 1999) as well as the radiative balance over the Atlantic, via scattering and absorption of solar radiation (and to a lesser extent absorption of terrestrial radiation), and microphysical and thermodynamical effects on clouds (Kaufman et al., 2005), and tropical cyclone formation (Evan et al., 2006). The dominant mode of coupled ocean-atmosphere variability in the tropical Atlantic is called Atlantic Meridional Mode (AMM). Evan et al. (2011) show that this mode is linked to Saharan dust variability. The AMM is thermally damped, thus direct ocean cooling from dust is required for the AMM to persist.

Along the western coast of Africa, extensive regions referred to as the semipermanent subtropical marine stratocumulus sheets exist, in which the stratocumulus cover exceeds 40% and can be as high as 60%. Therefore, they may be affected by the high concentrations of continental aerosols, in particular dust. Stratocumulus clouds strongly reflect incoming solar radiation (Chen et al., 2000) and exert only a small effect on the outgoing longwave radiation. Overall they exert a strong negative net radiative effect that markedly affects Earth's radiative balance (Stephens and Greenwald, 1991; Hartmann et al., 1992). Small changes in the coverage and thickness of stratocumuli are enough to produce a radiative effect comparable to that associ-

ated with increasing greenhouse gases (Randall et al., 1984; Slingo, 1990). A few observational studies show a relation between dust aerosols and cloud cover. Mahowald and Kiehl (2003) show that there was a positive correlation between observed thin low cloud amount and mineral dust off the west coast of North Africa. Observations during a dust storm suggest smaller cloud droplets and suppressed precipitation over the eastern Mediterranean (Rosenfeld et al., 2001). In another study, rainfall and dust load in the West African Sahel exhibit a negative correlation, which is explained by a larger number of cloud condensation nuclei (CCN) when the dust load is high, distributing available cloud water over a large number of droplets, thus suppressing droplet growth and precipitation (Hui et al., 2008). Li et al. (2010) study the indirect effects of mineral dust on warm clouds during a Saharan dust-transport event. They show that clouds are affected strongly by dust and the effects segregate and vary systematically when classified by cloud precipitation regime, cloud top temperature, and liquid water path (LWP). For nonprecipitating clouds the estimated aerosol indirect effect (AIE) is -0.1 Wm^{-2} over all temperature bands. Further classification by LWP (for all LWP > 150 gm^{-2}) strengthens the AIE to approximately -0.2 Wm^{-2}. McComiskey et al. (2009) present an assessment of ACI from ground-based remote sensing under coastal stratiform clouds. They calculate ACI as the change in cloud droplet number concentration (N_d) with aerosol concentration for constant values of LWP. They show that the average ACI depends on the relative value of cloud LWP, methods for retrieving N_d, the aerosol size distribution, updraft velocity, and the scale and resolution of observations. Doherty and Evan (2014) show that over the tropical North Atlantic during summer, low cloud fraction increases by 3-10 % in response to high mineral dust loadings. Wang et al. (2010) compare dusty and pure cloud properties and radiative forcing over northwestern China (source region) and over the northwestern Pacific (downwind region). Dusty clouds are defined as clouds that extend into a dust plume environment (i.e., dust aerosols observed within 50 m of the cloud), while pure clouds are clouds having no dust aerosols within 500 m around them. They show that dust aerosols change the microphysical characteristics of clouds, reducing the cloud effective particle size and, possibly, cloud optical depth, LWP, and ice water path (IWP). They show that dust aerosols cause an instantaneous net cooling effect in the source and

downwind regions respectively. Huang et al. (2006) analyze the effect of dust storms on cloud properties and radiative forcing over Northwestern China from April 2001 to June 2004. Due to changes in cloud microphysics, the instantaneous net radiative forcing is increased from −161.6 Wm^{-2} for dust-free clouds to -118.6 Wm^{-2} for dust contaminated clouds. Kishcha et al. (2015) focus on tropical Atlantic Ocean (30° N to 30° S. They find that during a 10-year study period (July 2002—June 2012), in July, dust intrusions from the Sahara into the tropical Atlantic cause a significant cloud cover up to 0.8—0.9 in the Saharan Air Layer. They suggest that the increase in cloud cover could be explained by the formation of shallow stratocumulus clouds below the temperature inversion with the assistance of settling Saharan dust particles.

In this paper, we will show the importance of Saharan dust contributions to ACI off the coast of North Africa, and in particular, the importance of the SDE. Initial modeling studies found that the SDE causes a positive radiative forcing, thus warming the climate system (Hansen et al., 1997; Allen and Sherwood, 2010). Furthermore, Ackerman et al. (2000) show that when absorbing aerosol coincides with shallow broken clouds, the radiative heating of absorbing aerosol reduces the cloud cover and increases the absorption solar radiation at the surface, resulting in a net positive radiative forcing. However, more recent modeling studies show that when absorbing aerosol resides above the cloud top, it can stabilize the underlying layer, enhancing stratocumulus clouds (Koch and Del Genio, 2010; Allen and Sherwood, 2010). Johnson et al. (2004), using large eddy simulation experiments, show aerosols may also yield increased cloud cover and surface cooling under certain scenarios. Although few observational studies exist to corroborate these model results, Wilcox (2010) uses satellite data and shows that when smoke resides above stratocumulus clouds, the increased buoyancy of the air above the clouds inhibits the entrainment of dry air, which helps preserve humidity and cloud cover in the boundary layer. Similarly, Brioude et al. (2009) showed the overall effect of biomass burning was to enhance marine stratocumulus off the coast of California. Koren et al. (2004), however, show that Amazonian biomass burning suppressed satellite-based cumulus cloud cover.

Here we quantify the radiative effects of Saharan dust on North Atlantic MSc. We use observations from multiple sensors in the NASA A-Train satellite constellation from 2004 to 2012

to evaluate the complex processes inherent in aerosol-cloud systems and to obtain estimates of aerosol-cloud radiative forcing for dust and marine stratocumulus clouds, including the uncertainties. The NASA data include CloudSat radar observations co-located with aerosol and cloud properties from CALIPSO, CERES and ERA-Interim reanalysis data. We show that the SDE—relative to the first and second aerosol indirect effects—is the largest component of ACI, and is also responsible for a seasonal reversal in the sign of ACI. A description of our datasets and methodology are provided in Sections 2 and 3. Results are presented in Section 4, and a discussion/conclusion is presented in Section 5.

2.2 Method

2.2.1 Study Area

Our study area is the tropical North Atlantic, defined between 45°W and 15°E, and 0-35°N. The boundaries of our study area are based on the location of the MSc regime and high dust load over the North Atlantic Ocean. Figure 2.1 shows DAOD from MACC for different seasons. During winter (December-January-February), dust is found within 0-15 °N off western Africa, over the North Atlantic Ocean. In summer (June-July-August), dust moves farther northward, occurring off the western coast of Africa between 10-25°N. During spring (March-April-May) and fall (September-October-November), dust is located between its wintertime and summertime locations. The maximum westward dust transport, as well as the maximum dust loading, occur during summer, with relatively high dust load out to ∼45°W.

A cloud regime based analysis is used to identify marine stratocumulus clouds (Medeiros and Stevens, 2011). The MSc regime is defined as 500 hPa vertical velocity $> 10hPa\ day^{-1}$ and to separate trade-wind cumuli from MSc, a LTS criterion is used, defined as $LTS = \Theta_{700hPa} - \Theta_{1000hPa} > 18.55K$ (where Θ is the potential temperature). Only grid points and days within the MSc regime are used in the analysis. Retrievals over bright surfaces like deserts are unreliable, so land areas are excluded. Figure 2.2 shows the percent of days in which the stratocumulus regime exists. During summer, between 10-40°N and 10-45° W, MSc occur from 50% to 80% of the

days. The percent of days the MSc regime occurs, is lower during the other seasons—particularly during fall—but the location is similar.

2.2.2 Satellite Methodology

Rosenfeld et al. (2014) show that when r_e reaches about 14 μm the coalescence accelerates and initiates warm rain. We only focus on non-raining clouds ($r_e < 14\ \mu m$), because under raining conditions, the relationship between cloud properties and DAOD may be subject to aerosol removal by precipitation and thus more difficult to analyze directly. Following Quaas et al. (2006), thin clouds with cloud optical thickness less than 4 and cloud effective radius less than 4 μm are excluded since neither a clear distinction between aerosols and clouds, nor an accurate retrieval of cloud properties is reliable in such cases.

N_d is estimated using the adiabatic approximation (Brenguier et al., 2000). This relationship assumes that liquid water content and cloud droplet radius increase monotonically with height in the cloud with a constant N_d in the vertical. Hence, N_d can be computed from cloud optical depth and r_e:

$$N_d = \gamma \tau_c^{1/2} r_e^{-5/2} \tag{2.1}$$

where τ_c is cloud optical depth, with $\gamma = 1.37 \times 10^{-5} m^{-0.5}$ (Quaas et al., 2006). Table 2.1 shows variables with their definitions used in the equations. Quaas et al. (2008) show that the planetary albedo (α) is described by contributions of clear and cloudy parts of the scene. They use a combination of CERES and MODIS products for a sigmoidal fit to describe the albedo of a cloudy scene involving liquid water clouds and extend it to include the clear part of the scene, where the planetary albedo also depends on the AOD. We use this approach to define the planetary albedo:

$$\alpha \approx (1-f)[a_1 + a_2 \ln \tau_a] + f_{liq}[a_3 + a_4 (f\tau_c)^{a_5}]^{a_6} + f_{ice}\alpha^{icecld} \tag{2.2}$$

where τ_a is aerosol optical depth, f is the fraction of all clouds including both liquid water and ice clouds ($f = f_{liq} + f_{ice}$), and α^{icecld} is the planetary albedo for the parts covered by ice clouds. a_1 - a_6 are fitting parameters taken from Quaas et al. (2008). The first term on the right hand side of this expression refers to planetary albedo in the clear sky and the second term describes the cloudy parts of the scene. The last term shows the contribution of ice clouds to the planetary albedo. Since we are interested in the effect of dust on MSc (which are warm clouds), $f = f_{liq}$ in this study and the last term can be neglected.

Aerosol index (AI= aerosol optical depth × Angström exponent) is derived from MACC and is used as a proxy for column CCN. The Angström parameter is defined as:

$$\beta = -\frac{\ln(\frac{AOD_{\lambda_1}}{AOD_{\lambda_2}})}{\ln(\frac{\lambda_1}{\lambda_2})} \tag{2.3}$$

The Angström exponent is calculated on the basis of AOD at 0.55 μm and 0.865 μm (Remer et al., 2005). It provides information on the particle size; the larger the exponent, the smaller the average size of the particles. The AI gives lower weight to large aerosols and reduces the impact of large but low number-concentration sea salt and dust particles (Stier, 2016). Liu and Li (2014) find improved correlation between surface CCN and AI as compared to AOD. Figure 2.3 shows the spatial pattern of the Angström exponent for different seasons. It has smaller values over North Africa and the neighboring ocean, indicating larger particles (dust) reside there.

To estimate the aerosol cloud radiative effect, statistical relationships between dust and clouds are calculated, following Quaas et al. (2008) (Method 1) and Chen et al. (2014) (Method 2) respectively. In Method 1, the radiative effect is decomposed into the first AIE and the combination of the second aerosol indirect effect (the cloud lifetime effect (CLE)) and the semi-direct effect. The first aerosol indirect radiative effect, or the cloud albedo effect, is calculated as the change in N_d to the change in AI:

$$AIE = f \cdot A(f, \tau_c)\frac{1}{3}\frac{d\ln N_d}{d\ln(AI)}[\ln\tau_a - \ln(\tau_a - \tau_{dust})]\overline{F}\downarrow \tag{2.4}$$

The second part corresponds to the combination of the CLE and the SDE, and includes both changes in LWP and cloud fraction to the change in AI:

$$CLE + SDE = (\alpha - (a_1 + a_2 \ln \tau_a)) \frac{d \ln f}{d \ln(AI)} [\ln \tau_a - \ln(\tau_a - \tau_{dust})] \overline{F} \downarrow \tag{2.5}$$

where f is the marine stratocumulus cloud coverage and clouds are not obscured by overlying ice clouds (i.e. the small number of scenes with ice clouds in our study area are removed from the analysis). $\bar{F} \downarrow$ is the mean daily downward solar radiation flux at the top of the atmosphere, in Wm^{-2}, as a function of the latitude and the day of the year. α is the planetary albedo, N_d is the liquid CDNC, τ_a is the AOD and τ_{dust} is the DAOD. A detailed description of the computation of equations (3-5), and $A(f, \tau_c)$ are given in the Appendix of Quaas et al. (2008).

In Method 2 the aerosol radiative effect includes the intrinsic effect (i.e., aerosol variations on cloud albedo, the combination of changes in cloud droplet size and LWP on cloud albedo) and the extrinsic effect (i.e., aerosol variations on fractional cloud cover). The aerosol radiative effect is calculated as the change in clear sky and cloud albedo, to the change in AI plus the change of cloud fraction to a change in AI:

$$RF = [\overline{C_m}(\frac{dA_{clr}}{d \ln(AI)} - \frac{dA_{cld}}{d \ln(AI)}) + (\overline{A_{clr} - A_{cld}}) \frac{df_{cld}}{d \ln(AI)}][\ln \tau_a - \ln(\tau_a - \tau_{dust})] \overline{F} \downarrow \tag{2.6}$$

Where $\overline{C_m}$ is the seasonal mean marine stratocumulus cloud coverage, A_{clr} is clear-sky albedo, and A_{cld} is the cloudy-sky albedo. The cloudy-sky albedo is derived using:

$$A_{cld} = [\alpha - (1 - f) A_{clr}] / f \tag{2.7}$$

The first and second term on the right hand side of eq. (6) are called the intrinsic and extrinsic effect respectively. Method 2 is an alternative way to estimate the total radiative effect which can be compared to Method 1. Contrary to Method 1, it is not possible to decompose the

total aerosol-cloud radiative effect into the AIE and the combination of CLE and SDE. Thus we only compare the total aerosol radiative effect estimated by these two methods.

To estimate the aerosol cloud radiative effect, linear regressions of each partial derivative are calculated. Each data point in the regression represents a day for which both dust and MSc data exist for the grid point. The sensitivities and radiative effects are calculated on a 1°×1° grid. In both methods, sensitivities with fewer than ten contributing data points are excluded. The uncertainty is computed from one-sigma error of the linear regression fit.

Gryspeerdt et al. (2016) show that by including information about N_d, the impact of the meteorological covariations in the susceptibility analysis is significantly reduced and much of the correlation between AOD and cloud fraction is explained by other factors than that mediated by N_d. They show that by considering these, the strength of the global mean relationship of AOD and cloud fraction is reduced by around 80%. We follow their new method and calculate this relationship as follows:

$$\frac{df}{d\ln(AI)} = \frac{df}{d\ln N_d} \cdot \frac{d\ln N_d}{d\ln(AI)} \tag{2.8}$$

2.3 Results

Here we present the annual and seasonal radiative effect of dust on MSc, as estimated by both Method 1 and Method 2. The annual mean aerosol cloud radiative effect estimated by Method 1 is -1.5 ± 1.4 Wm^{-2} (Table 2.2). The negative radiative effect indicates that dust modifies MSc in a way that results in a cooling effect over the study area. Method 1 separates the aerosol cloud radiative effect into two terms (Equations 4 and 5). Figure 2.4 shows the first aerosol indirect effect for different seasons. In all figures white areas indicate missing values, where no data for dust or clouds exist, or insufficient data exists to calculate the partial derivatives.

The first indirect effect is stronger where the dust load is larger and the stratocumulus regime exists for a longer time (see Figures 2.1 and 2.2). The annual mean first indirect effect is -0.3 ± 0.3 Wm^{-2}, and it varies from -0.7 ± 0.6 Wm^{-2} in summer to 0.1 ± 0.5 Wm^{-2} in winter

(Table 2.2). The larger negative radiative effect during summer, compared to spring and fall, is consistent with a greater abundance of both MSc and dust during summer.

Figure 2.5 shows the combination of the CLE and SDE (i.e., the second term in Method 1). Similar to the cloud albedo effect, the CLE + SDE is negative during summer, fall and spring and positive during winter. Moreover, CLE + SDE also exhibits a summertime maximum (negative), which is again consistent with the greater abundance of MSc and dust during summer. For all seasons the second term is much larger than the first term. The second term varies from -3.2 ± 2.5 Wm^{-2} in summer to 0.9 ± 2.9 Wm^{-2} in winter, with an annual mean of -1.2 ± 1.4 Wm^{-2}. This shows the importance of CLE and SDE in the study area.

Method 2 yields similar conclusions on the magnitude of the total aerosol cloud radiative effect, as well as the seasonal variation. The annual mean aerosol cloud radiative effect for Method 2 is -1.5 ± 1.6 (Table 2.2), and it varies from -4.3 ± 4.1 in summer to 0.6 ± 1 in winter. Method 2 separates the radiative effect into intrinsic and extrinsic parts, which are shown in Figure 2.6 and 2.7, respectively. The intrinsic effect dominates the radiative effect in this method. Like Method 1 the radiative effect is more negative over areas with larger dust load and a higher percentage of days with MSc.

The aerosol-cloud radiative effect is weakly positive during boreal winter. The presence of non-dusty aerosols could also be a reason of the large uncertainty. Kishcha et al. (2015) show that, in winter, Saharan dust is not the predominant aerosol species over our study area. In winter non-dusty aerosols, such as carbonates (organic and black carbon), sea salt and sulfates also significantly contribute to the total AOD over the tropical North Atlantic. Absorbing aerosols, such as organic and black carbon, produce mainly a positive semi-direct radiative effect, similar to that dust of. Sulfates and sea salt, non-absorbing aerosols, produce a negative indirect radiative effect, acting as effective CCN. Thus, non-dusty aerosols, producing either positive or negative radiative effects, significantly contribute to the large uncertainty of the aerosol-cloud radiative effect in winter. In Method 1, CLE and SDE dominate the total aerosol-cloud radiative effect. Since the sign of the dust-cloud radiative effect is affected by the height of dust column (Huang et al., 2014), to investigate the role of the SDE over the region, we look at the vertical

profile of Saharan dust from CALIPSO. Figure 2.8 shows that during winter, most of the dust burden resides between 0-1 km. In contrast, during spring there are two peaks of Saharan dust: the large peak resides within the marine boundary layer (between 0-1km), and a smaller peak resides above the boundary layer. During summer, similar to spring, there are two peaks, but most of dust resides above the boundary layer. During fall the amount of dust is less than in other seasons and most of dust burden resides between 0-1 km, with some dust between 1-4 km. The horizontal solid and dashed red lines in Figure 2.8 are average CERES MSc cloud top heights ± one-sigma respectively for each season. The average cloud top heights in summer and spring are lowest with 1.9±0.43 km and 1.98±0.41 km respectively, and highest in winter and fall with 2.2±0.3 km as shown in Figure 2.9. CALIPSO shows that 88.3% ±8.5% of dust resides below 2.2 km in winter. During summer, however, there are two peaks, with 35.6% ±13% below 1.5 km and 44.4% ±9.2% between 2 and 4 km.

To be more clear we plot cloud top height for different seasons. Figure 2.9 shows the MSc cloud top height over the study area for all seasons. In summer for most of our study area the cloud top height is less than 2 km, while in winter it is more than 2 km. The cloud top height in spring and fall is between summer and winter. Since MSc form within the boundary layer, a considerable amount of dust resides above the clouds during summer. We use cloud top height for those days where the vertical profile of dust extinction coefficient from CALIPSO is available and calculate how much dust is above the top of MSc. The extinction coefficient of dust for each level is obtained from CALIPSO and vertically integrated to calculate DAOD for each grid box, and then extinction coefficients above the CERES cloud top heights are vertically integrated and divided by DAOD to give the percent of dust above the clouds. The computation is done on a $1^\circ \times 1^\circ$ grid. Figure 2.10 shows that 61.8% ±12.6 of the dust resides above MSc during the summer; only 11.9% ±10.8 resides above MSc during the winter. In spring (fall) 35% ±19.8% (31.2% ±15.9%) of the dust resides above MSc. Tsamalis et al. (2013) show that during the summer, the Saharan air layer is found to be thicker and higher near Africa at 1-5 km. During winter, it occurs in the altitude range 0-3 km off the western Africa. This is consistent with the vertical profile of Saharan dust in our study. This vertical profile analysis helps to explain the

relatively weak first term of Method 1, relative to the second term.

To investigate this more, we plot the two partial derivatives that constitute the second term of Method 1. Figure 2.11 and 2.12 show the sensitivity of the cloud fraction and LWP to a relative change in AI for all seasons. Using equation (8) to calculate the sensitivity of cloud fraction to a relative change in aerosol index leads to a non-linear distribution, thus the statistical significance of the equation (8) is evaluated using a bootstrap test. Note that by using equation (8) (i.e. only cloud fraction changes mediated by Nd) the effect of absorbing aerosol on meteorology and subsequently cloud cover is suppressed (i.e. a part of the SDE). Figure 2.11 shows that the sensitivity of cloud fraction to AI is relatively weak. It also shows that this sensitivity is positive (negative) during summer (winter) for most of the study area, which shows that cloud fraction increases (decreases) when AI increases. Figure 2.12 shows that the sensitivity of LWP to AI dominates the second term of Method 1. During winter, most of the study area features a reduction in LWP with respect to the AI. During summer, however, this sensitivity is generally positive. Considering the seasonal contrast in the amount of dust above MSc during summer versus winter, the seasonal reversal of these sensitivities—which drive the reversal in the total aerosol cloud radiative effect—is consistent with the importance of the SDE.

Since the bulk of the dust resides above MSc during summer, aerosol-cloud microphysical interactions (including AIE and CLE) would be muted. Thus, AIE and CLE would be smaller than SDE. Moreover the SDE would be negative, as observed by the CLE+SDE term of Method 1. Wilcox (2010) also shows that absorbing aerosols overlying MSc largely do not interact with the clouds. However, the aerosols still result in cloud thickening by a dynamical feedback related to the enhanced stability of the atmosphere, which yields an increase in the cloud albedo. This is consistent with Koch and Del Genio (2010), who show that absorbing aerosol above MSc result in increased stability, which strengthens the inversion, and reduces cloud-top entrainment of the overlaying dry air, thereby enhancing the underlying clouds. Kok et al. (2017) show that the dust found in the atmosphere is substantially coarser than represented in current global climate models. As coarse dust warms the climate, the temperature inversion is stronger and yields thickening of the underlying clouds. Doherty and Evan (2014) show that in response to

increased dust load over the tropical North Atlantic in summer, MSc also increase, and this is linked to increases in atmospheric stability, reductions in boundary layer height, and moistening of the lower atmosphere.

During winter, when the total aerosol cloud radiative effect reverses sign and becomes positive, most of dust burden resides within or below the clouds. When absorbing aerosol coincides with the cloud, the heating favors cloud clearing and thinning, thus reducing the cloud albedo and yielding a positive radiative effect (Hansen et al., 1997; Johnson et al., 2004). In contrast, aerosol indirect effects do not drive cloud clearing/thinning, and thus do not contribute a positive radiative effect. Therefore, over our study area, we conclude that the SDE is the most important aerosol-cloud effect resulting in an overall negative radiative effect. The SDE is also strong enough to change the sign of total aerosol cloud radiative effect from negative to positive during the winter.

2.4 Conclusions

To estimate the aerosol-cloud radiative effect of Saharan dust on North Atlantic MSc , we use observational data from several different satellites from 2004 to 2012. The aerosol-cloud radiative effect is estimated using two different methods, following Quaas et al. (2008) (Method 1) and Chen et al. (2014) (Method 2). The annual mean aerosol cloud radiative effect estimated by Method 1 is -1.5 ± 1.4 Wm^{-2}. Estimating the radiative effect using Method 2 yields similar results, with an annual mean of -1.5 ± 1.6 Wm^{-2}. Thus, both methods show that Saharan dust modifies MSc in a way that has a cooling effect over the North Atlantic Ocean. Both methods also yield a seasonal maximum negative radiative effect during summer, which is consistent with more Saharan dust and MSc during summer. Furthermore, both methods yield a reversal in the sign of the aerosol cloud radiative effect, which switches from negative to positive during the winter season. In Method 1, the radiative effect varies from -3.8 ± 2.5 Wm^{-2} during summer to 1 ± 2.9 Wm^{-2} during winter; similarly, Method 2 varies from -4.3 ± 4.1 during summer to 0.6 ± 1 during winter. Method 1 allows us to separate the cloud albedo effect (first term of Method 1)

from the CLE and the SDE (second term of Method 1). The cloud albedo effect, which varies from -0.7 ± 0.6 Wm^{-2} in summer to 0.1 ± 0.5 Wm^{-2} in winter and is relatively small compared to the CLE+SDE, which varies from $-3.2\ \pm2.5$ Wm^{-2} in summer to 0.9 ± 2.9 Wm^{-2} during winter. This shows the importance of the second term, the combination of the CLE and the SDE.

To gain insight as to whether CLE or SDE dominates the second tern of Method 1, we use CALIPSO data to quantify the amount of Saharan dust that resides above MSc. The analysis shows that 61.8%±12.6% of Saharan dust resides above MSc during summer, but only 11.9% ±10.9% resides above MSc during winter. This seasonal dependence in the location of the dust, relative to MSc, shows the importance of the SDE.

When most dust resides above the clouds during summer, aerosol-cloud microphysical effects that involve the co-location of aerosol and cloud, such as the second aerosol indirect effect (CLE), would likely be muted relative to the SDE. Moreover, the positive value of the aerosol-cloud radiative effect during winter, when most dust resides within MSc, indicates that the SDE is dominant— that is the only mechanism by a negative aerosol-cloud radiative effect can be obtained. We conclude that aerosol-cloud radiative effects associated with Saharan dust and North Atlantic MSc are dominated by the semi-direct effect.

Table 2.1: A summary of notation used for equations in this paper

Symbol	Meaning
N_d	Cloud droplet number concentrations
α	Planetary albedo
f	Total cloud fraction including both liquid water and ice cloud fraction
f_{ice}	Ice cloud fraction
f_{liq}	Liquid water cloud fraction
τ_a	Aerosol optical depth
τ_c	Cloud optical depth
τ_{dust}	Dust aerosol optical depth
r_e	Effective cloud-particle radius
LWP	Liquid water path
A_{cle}	Clear-sky albedo
A_{cld}	Cloudy-sky albedo
$\overline{C_m}$	Seasonal mean MSc
$\bar{F}\downarrow$	daily mean solar radiation at TOA
AI	Aerosol Index

Table 2.2: Seasonal and annual radiative effects estimated by Method 1 (Quaas et al., 2008) and Method 2 (Chen et al., 2014).

	Method 1			Method 2
	AIE	CLE+SDE	Total radiative Effect	Total radiative Effect
Winter	0.1±0.5	0.9±2.9	1±2.9	0.6±1
Spring	-0.03±0.9	-1.38±3.1	-1.4±3.2	-1.3±3.9
Summer	-0.7±0.6	-3.2±2.5	-3.8±2.5	-4.3±4.1
Fall	-0.38±0.5	-1.2±2.4	-1.58±2.4	-1±2.5
Annual	-0.3±0.3	-1.2±1.4	-1.5±1.4	-1.5±1.6

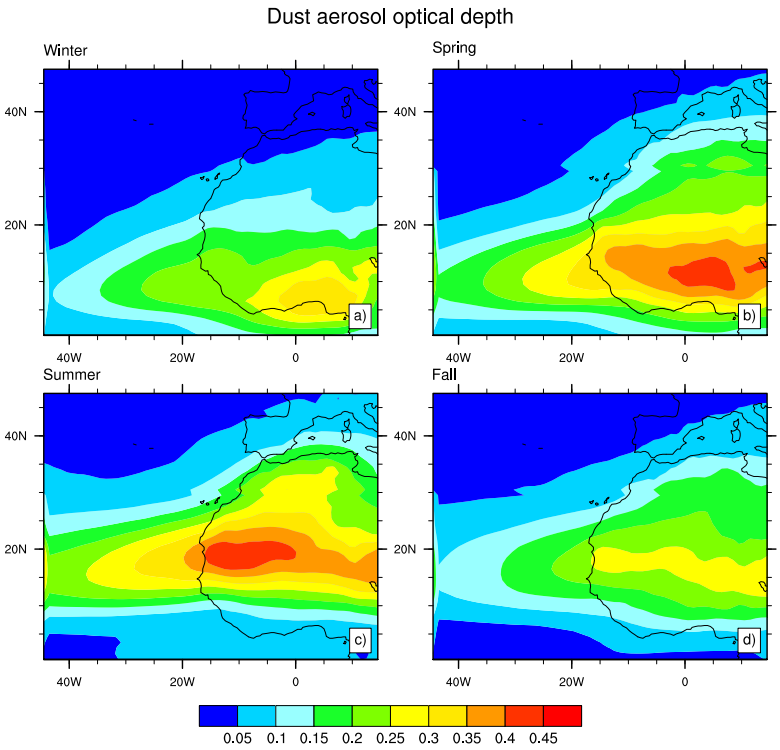

Figure 2.1: MACC dust aerosol optical depth (DAOD) from 2004-2012 in (a) winter, (b) spring, (c) summer, and (d) fall.

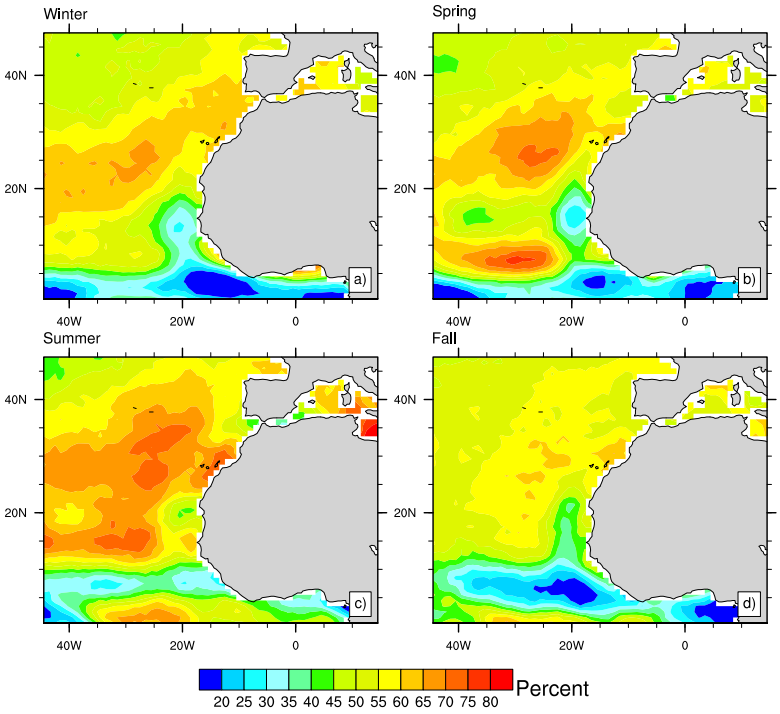

Figure 2.2: Percent of days from 2004-2012 in which marine stratocumulus clouds are found following Medeiros and Stevens (2011) in (a) winter, (b) spring, (c) summer, and (d) fall.

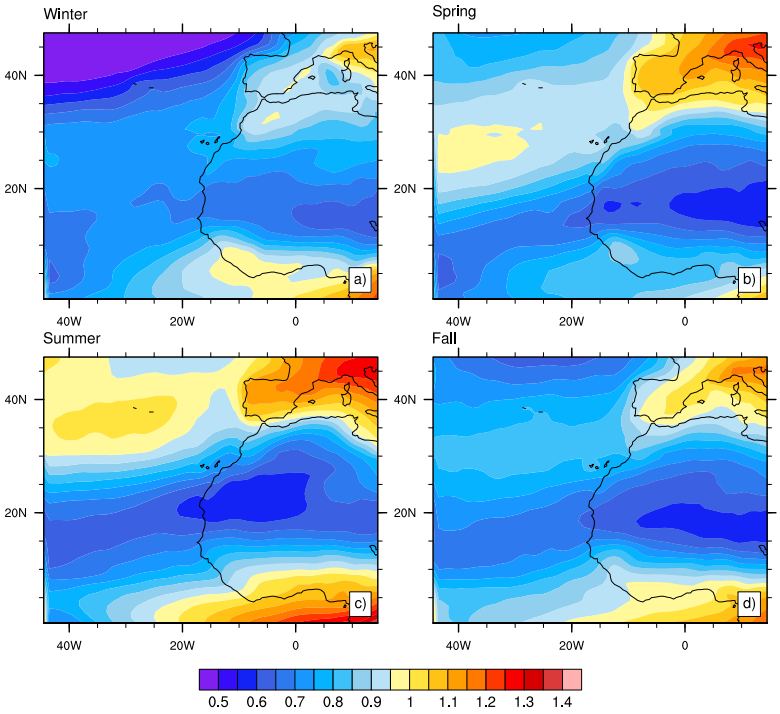

Figure 2.3: Aerosol Ängström exponent from MACC in (a) winter, (b) spring, (c) summer, and (d) fall.

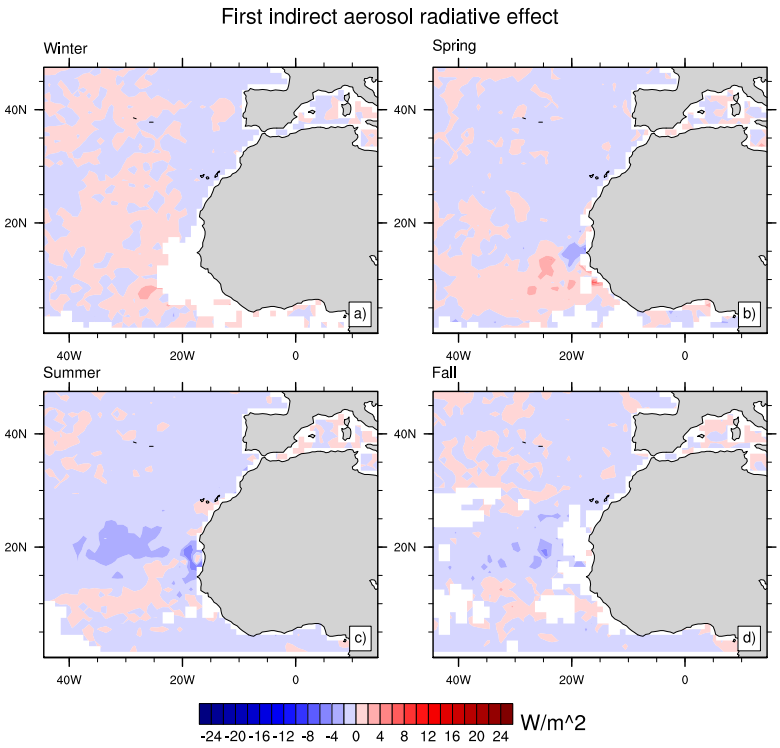

Figure 2.4: Fist indirect radiative effect (cloud albedo effect) of dust on marine stratocumulus clouds (Wm^{-2}) following Quaas et al. (2008) for (a) winter, (b) spring, (c) summer, (d) fall.

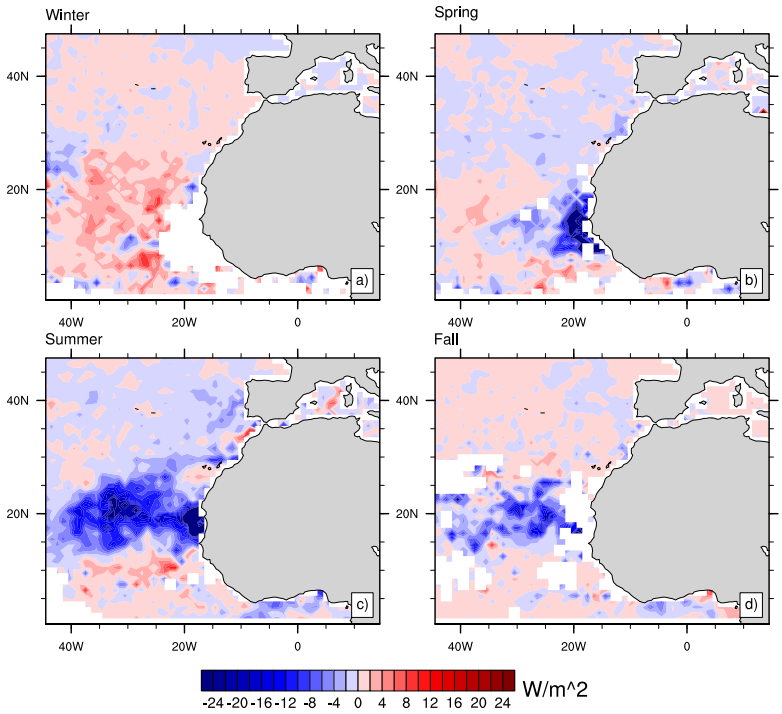

Figure 2.5: The second term of Method 1 (Quaas et al., 2008), which represents the cloud lifetime effect and semi-direct effect of dust on marine stratocumulus clouds (Wm^{-2}) which includes CLE+SDE for (a) winter, (b) spring, (c) summer, (d) fall.

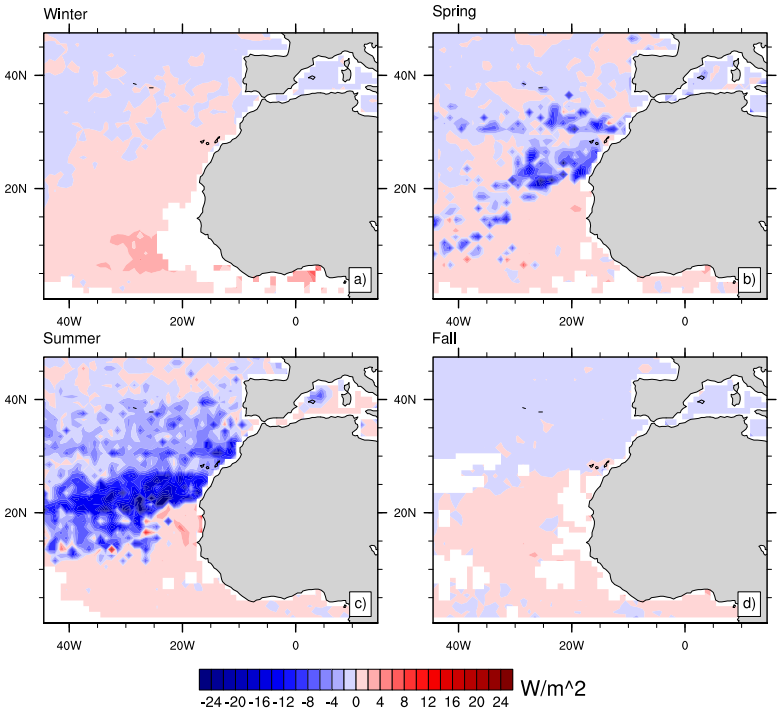

Figure 2.6: The intrinsic aerosol cloud radiative effect estimated for marine stratocumulus clouds ($W\,m^{-2}$) following Chen et al. (2014) for (a) winter, (b) spring, (c) summer, (d) fall.

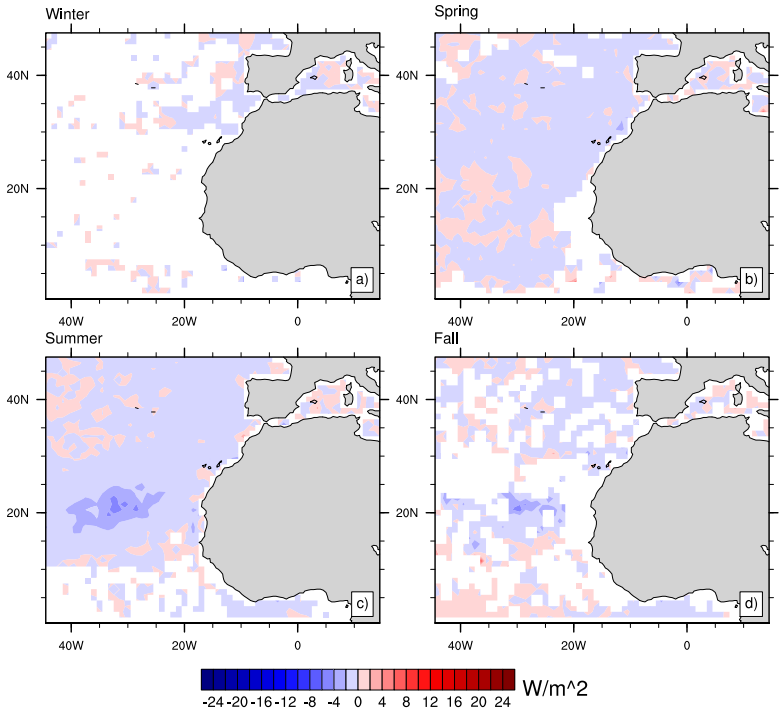

Figure 2.7: The extrinsic aerosol cloud radiative effect (Wm^{-2}) following Chen et al. (2014) for (a) winter, (b) spring, (c) summer, (d) fall.

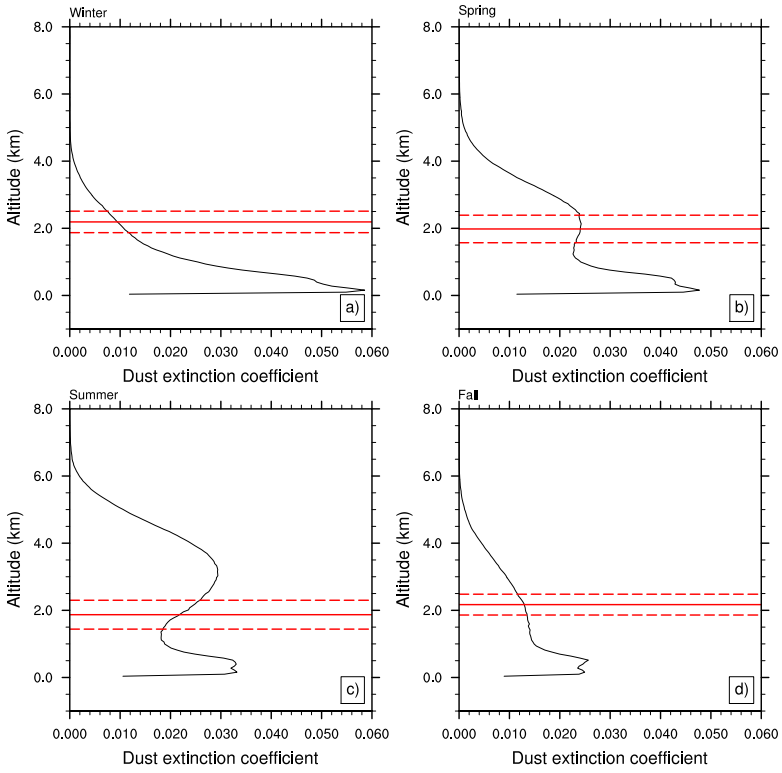

Figure 2.8: Vertical profile of the dust extinction coefficient from CALIPSO in (a) winter, (b) spring, (c) summer, (d) fall. Solid and dashed red lines show CERES MSc cloud top height ± one-sigma for each season.

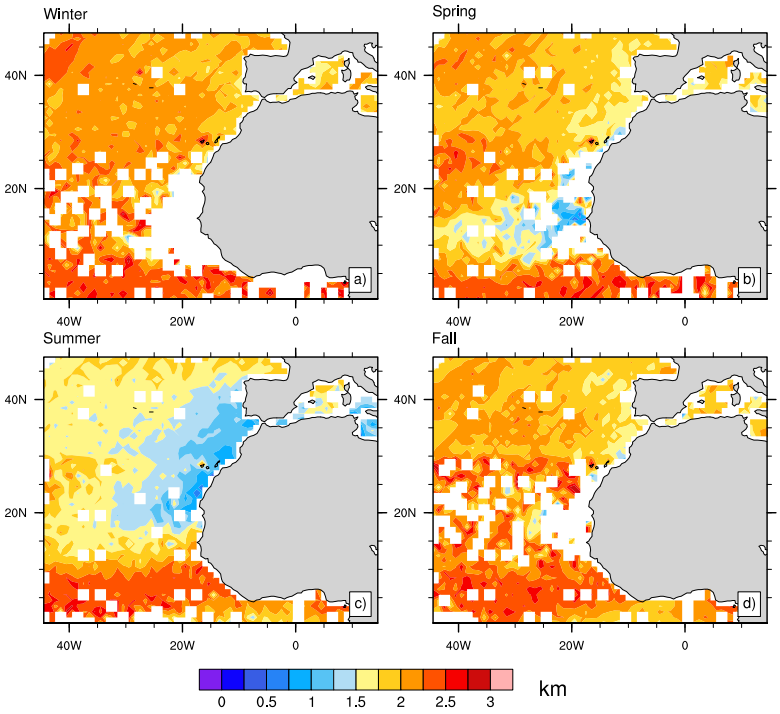

Figure 2.9: Marine stratocumulus cloud top height from CERES in (a) winter, (b) spring, (c) summer, (d) fall.

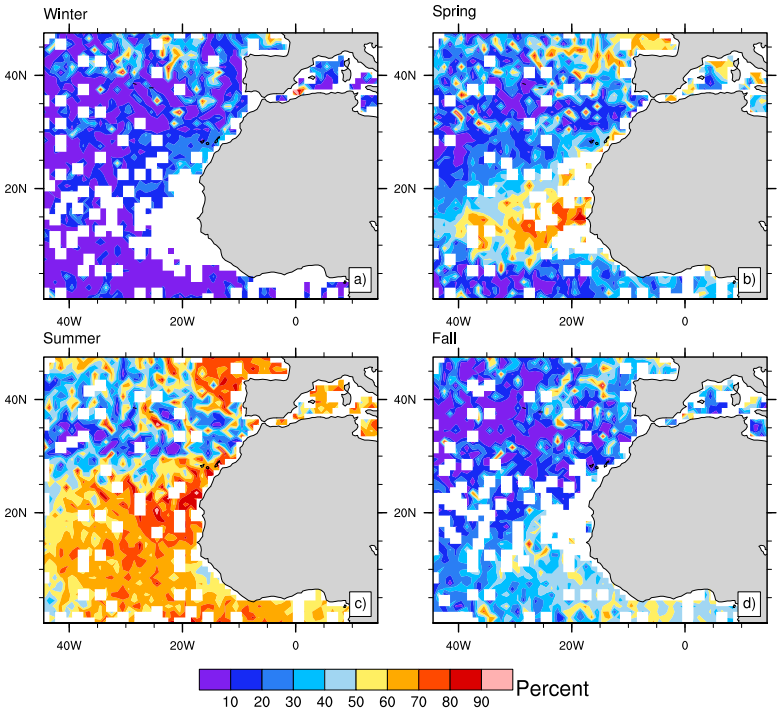

Figure 2.10: Amount of dust (%) above marine stratocumulus clouds in (a) winter, (b) spring, (c) summer, (d) fall.

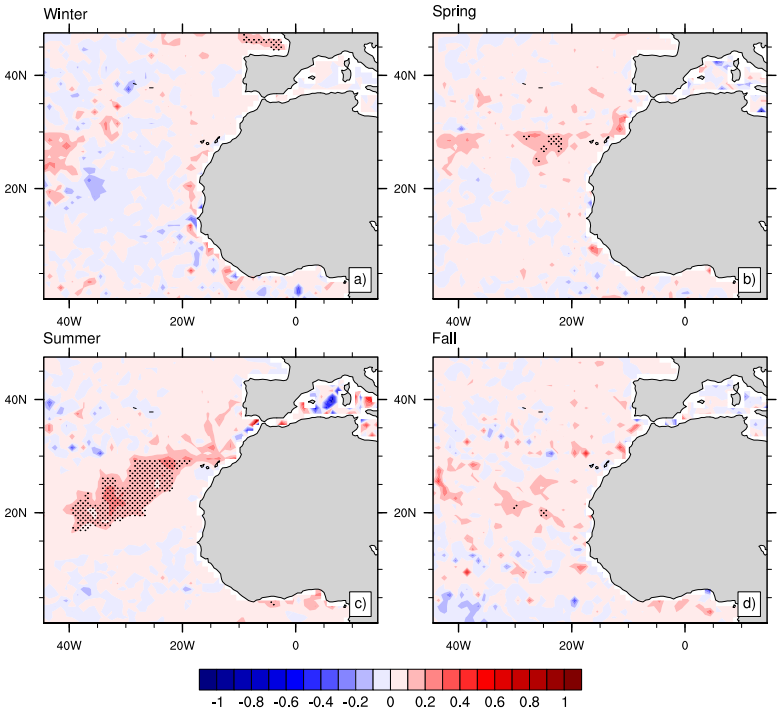

Figure 2.11: The sensitivity of cloud fraction to a relative change in aerosol index for (a) winter, (b) spring, (c) summer, (d) fall. Dots represent the significance at 95% confidence level.

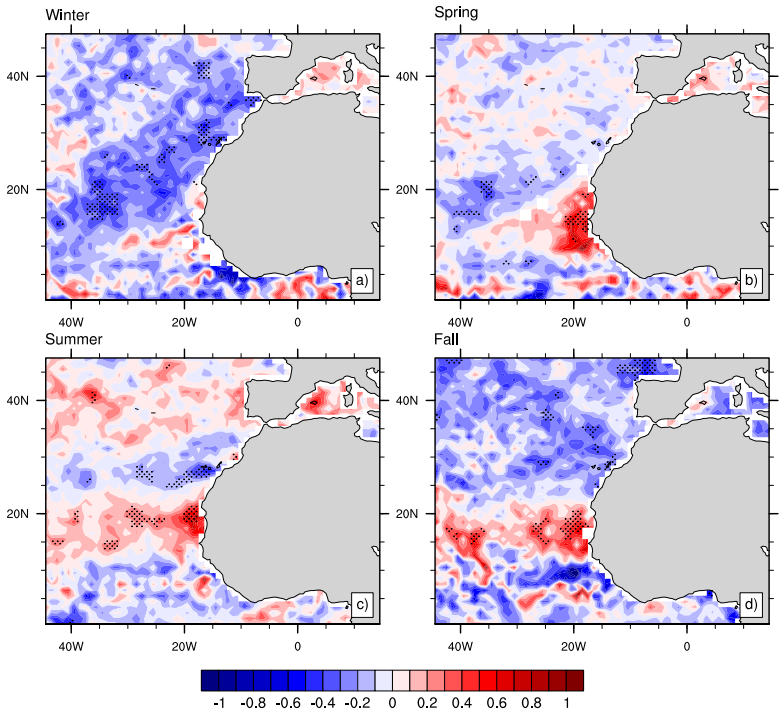

Figure 2.12: The sensitivity of liquid water path to a relative change in aerosol index for (a) winter, (b) spring, (c) summer, (d) fall. Dots represent the significance at the 95% confidence level.

Chapter 3

Aerosol-cloud semi-direct effects enhance warming of the climate system

Abstract

Absorbing aerosols like black carbon (BC) give rise to rapid adjustments and the associated perturbation to the atmospheric temperature structure alters the cloud distribution. These "semi-direct effects" (SDEs) depend on the vertical co-location of absorbing aerosol and cloud (Koch and Del Genio, 2010; Bond et al., 2013; Amiri-Farahani et al., 2017), and include relative humidity reductions and cloud burn-off when BC and cloud are co-located (Hansen et al., 1997; Ackerman et al., 2000), but also enhanced low-level cloud due to increases in stability when BC is located above the cloud (Johnson et al., 2004; Allen and Sherwood, 2010; Koch and Del Genio, 2010; Perlwitz and Miller, 2010; Randles et al., 2013). The level of scientific understanding of the SDE is considered low, with models indicating a likely negative (−0.44 to +0.1 Wm^{-2}) forcing (Bond et al., 2013). Recent studies suggest this negative SDE is primarily driven by decreases in high-level clouds and enhanced longwave cooling (Mahajan et al., 2013; Hodnebrog et al., 2014; Sand et al., 2015; Stjern et al., 2017). Here, we investigate

the SDE using multiple models driven by observationally constrained fine-mode aerosol forcing without dust and sea salt (Chung et al., 2016). Unlike aerosol simulations, which yield a relatively vertically uniform aerosol atmospheric heating profile with significant upper-tropospheric heating, observation-based heating peaks in the lower-troposphere and then decays to zero in the mid-troposphere. We find a significant global annual mean decrease in low and mid-level clouds, and weaker decreases in high-level clouds, which leads to a positive SDE dominated by shortwave radiation. Thus, in contrast to most studies, we find a robust positive SDE, implying rapid adjustments act to warm the climate system. Sensitivity tests with identical, but vertically uniform observationally-constrained aerosol atmospheric heating result in a negative SDE, due to enhanced longwave cooling as a result of large reductions in high-level clouds. Our results therefore suggest that model simulations lead to a negatively biased SDE, due to an aerosol atmospheric heating profile that is too vertically uniform. Absorbing aerosols like black carbon (BC) give rise to rapid adjustments and the associated perturbation to the atmospheric temperature structure alters the cloud distribution. These "semi-direct effects" (SDEs) depend on the vertical co-location of absorbing aerosol and cloud (Koch and Del Genio, 2010; Bond et al., 2013; Amiri-Farahani et al., 2017), and include relative humidity reductions and cloud burn-off when BC and cloud are co-located (Hansen et al., 1997; Ackerman et al., 2000), but also enhanced low-level cloud due to increases in stability when BC is located above the cloud (Johnson et al., 2004; Allen and Sherwood, 2010; Koch and Del Genio, 2010; Perlwitz and Miller, 2010; Randles et al., 2013). The level of scientific understanding of the SDE is considered low, with models indicating a likely negative (-0.44 to $+0.1$ Wm^{-2}) forcing (Bond et al., 2013). Recent studies suggest this negative SDE is primarily driven by decreases in high-level clouds and enhanced longwave cooling (Mahajan et al., 2013; Hodnebrog et al., 2014; Sand et al., 2015; Stjern et al., 2017). Here, we investigate the SDE using multiple models driven by observationally constrained fine-mode aerosol forcing without dust and sea salt (Chung et al., 2016). Unlike aerosol simulations, which yield a relatively vertically uniform aerosol atmospheric heating profile with significant upper-tropospheric heating, observation-based heating peaks in the lower-troposphere and then decays to zero in the mid-troposphere. We find a significant global

annual mean decrease in low and mid-level clouds, and weaker decreases in high-level clouds, which leads to a positive SDE dominated by shortwave radiation. Thus, in contrast to most studies, we find a robust positive SDE, implying rapid adjustments act to warm the climate system. Sensitivity tests with identical, but vertically uniform observationally-constrained aerosol atmospheric heating result in a negative SDE, due to enhanced longwave cooling as a result of large reductions in high-level clouds. Our results therefore suggest that model simulations lead to a negatively biased SDE, due to an aerosol atmospheric heating profile that is too vertically uniform.

3.1 Introduction

Unlike other climate change drivers, the temperature and cloud response—and in some cases, the precipitation response (Samset et al., 2016)—to absorbing aerosol is dominated by rapid adjustments (Stjern et al., 2017). Recent studies show that these adjustments, which include the aerosol-cloud semi-direct effect (SDE), lead to a negative radiative perturbation, thereby offsetting some of the positive direct forcing of absorbing aerosol, resulting in a relatively weak surface temperature response (Myhre et al., 2017; Stjern et al., 2017). Climate models from the Precipitation Driver Response Model Intercomparison Project (PDRMIP) show that a ten-fold increase in BC leads to a robust increase in globally averaged low-level cloud (CLOW), but a reduction in mid-level (CMED) and in particular, high-level (CHI) cloud (Stjern et al., 2017). Qualitatively similar cloud responses are obtained in several other recent studies (Mahajan et al., 2013; Hodnebrog et al., 2014; Sand et al., 2015). Consistent with these cloud changes, and in particular the large CHI reduction and enhanced longwave cooling, the annual global mean rapid adjustment in these simulations ranges from -0.39 to -1.44 W m^{-2} for a ten-fold increase in BC (Mahajan et al., 2013; Stjern et al., 2017); -2.8 W m^{-2} for 25×BC (Sand et al., 2015); and -0.25 W m^{-2} for present-day BC emissions (Hodnebrog et al., 2014). Thus, model simulations show that rapid adjustments—primarily due to cloud responses—offset up to 60% of the direct radiative forcing associated with BC (Stjern et al., 2017).

The climate impact of absorbing aerosols, however, is associated with significant uncertainty (Bond et al., 2013; Boucher et al., 2013). This is related to several factors, including underestimation of BC emission inventories and absorption aerosol optical depth, which implies too little aerosol solar absorption in the atmosphere and therefore, underestimation of BC direct radiative forcing (Ramanathan and Carmichael, 2008; Koch et al., 2009; Chung et al., 2012; Bond et al., 2013; Cohen and Wang, 2014; Myhre and Samset, 2015). The vertical profile of absorbing aerosol is also important, as it impacts the direct radiative forcing, as well as the rapid adjustments and precipitation response (Ming et al., 2010; Zarzycki and Bond, 2010; Bond et al., 2013; Koch et al., 2009; Koch and Del Genio, 2010; Ban-Weiss et al., 2012; Samset and Myhre, 2015). In the context of the aerosol-cloud SDE, different cloud responses are obtained depending on the vertical co-location of absorbing aerosol and cloud (Koch and Del Genio, 2010; Bond et al., 2013).

Large inter-model diversity exists in simulated BC vertical profiles, with models likely overestimating the amount of BC aloft (Koch et al., 2009; Schwarz et al., 2010; Bond et al., 2013; Allen and Landuyt, 2014). This could be related to a variety of factors, including vertical resolution (Koffi et al., 2016), convective processes (Allen and Landuyt, 2014; Park and Allen, 2015), scavenging (Garrett et al., 2010), or aging (Liu et al., 2011). Thus, given these uncertainties in aerosol simulations—particularly related to the vertical profile of absorbing aerosol—the corresponding aerosol-cloud SDE may not be properly constrained by the aforementioned studies.

Aerosol observations do not suffer systematic errors as much as aerosol simulations. Moreover, the aerosol vertical profile can be constrained through observations. Here we estimate the aerosol-cloud SDE using three different climate models (Methods), including the Community Atmosphere Model version 4 (CAM4) (Neale et al., 2010b) and CAM5 (Neale et al., 2010a), as well as the Geophysical Fluid Dynamics Laboratory (GFDL) Atmospheric Model version 2.1 (AM2.1) (Anderson et al., 2004), forced with observationally-constrained fine mode aerosols without dust and sea salt (Chung et al., 2016) (Methods; "STANDARD" simulations). We also conduct analogous observationally-constrained aerosol simulations, but with vertically uniform aerosol atmospheric heating ("VERTUNIF" simulations). Both are compared to PDRMIP 10xBC.

3.2 Methods

3.2.1 Global Climate Models

This study uses the National Center for Atmospheric Research (NCAR) Community Atmosphere Model version 4 (CAM4) (Neale et al., 2010b) and CAM5 (Neale et al., 2010a). Both models have a horizontal resolution of 1.9°x2.5°; CAM4 has 25 vertical layers and CAM5 has 30. Their main shared physical parameterization is the Zhang-McFarlane deep convection scheme (bulk mass flux with CAPE closure) (Zhang and McFarlane, 1995). CAM4 uses a shallow convection scheme that involves three-level adjustment of moist static energy (Hack, 1994) and a prognostic single-moment microphysics scheme, including diagnostic cloud fraction (Rasch and Kristjánsson, 1998). Cloud fraction depends on several factors, including RH, S, water vapor and convective mass fluxes. Three types of cloud are diagnosed: low-level marine stratus, convective cloud, and layered cloud. Layered clouds form when RH exceeds a pressure dependent threshold. Marine stratocumulus clouds are diagnosed using an empirical relationship based on S. Convective cloud fraction is related to updraft mass flux in the deep and shallow cumulus schemes. The remaining cloud types are diagnosed on the basis of relative humidity (Neale et al., 2010b).

CAM5 uses a mass flux scheme with convective inhibition closure for shallow convection (Park and Bretherton, 2009) and a prognostic double moment microphysics scheme (Morrison and Gettelman, 2008) with ice supersaturation (Gettelman et al., 2010) and a diagnostic cloud fraction scheme for cloud microphysics and macrophysics. Although deep cumulus cloud fraction is diagnosed as in CAM4, shallow cumulus fraction in CAM5 is directly computed using the definition of convective updraft mass flux from the new shallow convection scheme. Liquid stratus fraction is derived from the assumed triangular distribution of total relative humidity. The sensitivity of liquid stratus fraction to the changes of grid-mean RH differs between the two models. Ice stratus fraction is also diagnosed, using a modified version of Slingo's formula.

We also use the Geophysical Fluid Dynamics Laboratory (GFDL) Atmospheric Model version 2.1 (AM2.1) (Anderson et al., 2004), with a horizontal resolution of 2°x2.5° and 24 vertical

layers. Moist convection is represented by the Relaxed Arakawa-Schubert formulation (Moorthi and Suarez, 1992). In this parameterization, convection is represented by a spectrum of entraining plumes which produce precipitation. Closure is determined by relaxing the cloud work function for each cloud in the spectrum back to a critical value over a fixed time scale. Large-scale clouds are parameterized with separate prognostic variables for specific humidity of cloud liquid and ice, with an updated treatment of mixed phase clouds (Rotstayn, 1997; Rotstayn et al., 2000). Stratocumulus cloud cover is based on large-scale subsidence, diabatic cooling by radiation, and turbulent entrainment of warm and dry air from above the inversionTiedtke (1993).

3.2.2 Experimental Design

We conduct experiments with fixed sea surface temperature (fSST), which uses a repeating cycle of monthly climatological SSTs. The fSST setup prohibits significant global mean temperature change while keeping fast atmospheric responses, like the SDE. Experiments are run for 20 years, and the last 15 years are used in this study. Monthly observationally-constrained fine-mode aerosol radiative effects (atmospheric heating rate and surface solar radiation reduction) are interpolated to each model's horizontal resolution and incorporated into their radiation modules. The atmospheric heating rate is vertically interpolated to each model's hybrid pressure levels. Although aerosol forcing is almost independent of solar zenith angle (θ) when the angle is small, aerosol forcing approaches zero as θ approaches 90°. Thus, the added aerosol radiative effect is multiplied by a scaling factor that depends on zenith angle (Chung, 2006; Allen and Sherwood, 2010). The climate response is estimated as the difference between the simulation with observationally constrained fine mode aerosol without dust and sea salt, and a corresponding control run without ("STANDARD" simulations). The idealized vertically uniform heating simulations ("VERTUNIF") are analogous, but the monthly mean aerosol atmospheric heating is vertically averaged at each grid box, and this vertically-averaged value is prescribed to all pressure levels <100 hPa.

3.2.3 Observationally-constrained Aerosol Forcing

Satellite aerosol optical depth (AOD) from the Moderate Resolution Imaging Spectroradiometer (MODIS) and Multi-angle Imaging SpectroRadiometer (MISR) is nudged towards the ground-based AErosol RObotic NETwork (AERONET) AOD (Chung et al., 2005; Lee and Chung, 2013). The AOD Angstrom exponent is also derived by adjusting the satellite data towards AERONET data. Fine-mode aerosol optical depth (fAOD) at 500 nm is obtained by using AERONET fAOD and total AOD to derive the fine-mode fraction (FMF). AOD Angstrom exponent data is converted into FMF data, which is then nudged towards AERONET FMF data to derive reliable FMF and fAOD over the globe. Observational data gaps—which are primarily confined to polar regions—are filled by the Goddard Chemistry Aerosol Radiation and Transport (GOCART) model. Aerosol optical properties, such as the single scatter albedo (SSA) and asymmetry parameter (ASY), are obtained by nudging GOCART SSA and ASY towards AERONET data.

Aerosol vertical profiles are obtained from the space-borne Cloud-Aerosol Lidar with Orthogonal Polarization (CALIOP) (Liu et al., 2009). Daytime CALIPSO Level 2.0 data was processed to obtain a clear-sky aerosol extinction coefficient at 532 nm. Data gaps are filled using available neighboring data through linear interpolation. Aerosol vertical profile from CALIPSO is scaled to match the AOD observations obtained by integrating AERONET, MODIS and MISR data. To adjust the magnitude of AOD over cloud by CALIPSO data, daytime CALIPSO lidar Level 3.0 data (Winker et al., 2013) is used, specifically, the ratio of clear-sky AOD to above-cloud AOD. The direct aerosol effect is obtained by incorporated the integrated global aerosol data into the Monte-Carlo Aerosol Cloud Radiation (MACR) model. We note that although this approach uses observations to constrain the fine-mode aerosol radiative effect, the results are subject to observation errors. AERONET SSA, in particular, is subject to potentially significant uncertainties due to various assumptions used in the retrieval algorithms.

The global average atmospheric heating (F_{ATM}) and reduction in surface solar radiation (F_{SFC}) for fine mode aerosols without dust and sea salt, which include both natural and anthropogenic aerosols, is +3.64 W m^{-2} and −3.75 W m^{-2}, respectively (−0.11 W m^{-2} TOA forcing). These estimates are several times larger than anthropogenic forcings estimated from models

(Myhre et al., 2013), which are 0.75 W m^{-2} for F_{ATM} and −1.02 W m^{-2} for F_{SFC}. Furthermore, the observationally-constrained F_{ATM} and F_{SFC} are larger over land than oceans. F_{ATM} is 2.67 (5.82) W m^{-2} over ocean (land) and F_{SFC} is −2.99 (−5.47) over ocean (land).

3.2.4 Semi-direct Effect Calculation

We account for aerosol radiative effects by incorporating the surface solar radiation reduction and atmospheric solar heating of observationally-constrained fine-mode aerosol without dust and sea salt. This allows us to estimate the aerosol-cloud SDE using the traditionally defined cloud radiative flux (CRF)—the difference between top-of-the-atmosphere (TOA) net all-sky and clear-sky shortwave and longwave radiative fluxes. The SDE is the difference between the CRF from the observationally-constrained aerosol experiment and the control run. In the case of CAM4 from PDRMIP, one is unable to use the traditionally defined CRF, which leads to a positive shortwave bias in the case of absorbing aerosol (Ghan, 2013). Thus, it is necessary to us the clear sky cloud radiative forcing. Unfortunately, CAM4 is the only PDRMIP model to archive this diagnostic.

The effective radiative forcing (ERF) is estimated as the difference in TOA radiative fluxes between aerosol simulation and control. The instantaneous radiative forcing (IRF) is estimated by an additional diagnostic call to the radiation scheme, but neglecting the scattering and absorbing of aerosols. The IRF is then the difference in TOA radiative fluxes, with and without aerosol direct effects. Since ERF = IRF + RAP_{ADJ}, RAP_{ADJ} is estimated as ERF—IRF. Furthermore, IRF is negligible in the longwave, so $ERF_{LW} = RAP_{ADJ-LW}$. Rapid adjustments can be broken down into SDE + “residual", where residual is related to changes in temperature and moisture. As long as the SDE is known, the residual can be subsequently estimated as RAP_{ADJ} −SDE.

3.3 Results

Figure 3.1 shows the annual (ANN) mean atmospheric solar absoprtion (F_{ATM}) and reduction in surface solar radiation (F_{SFC}) for observationally-constrained fine mode aerosols without dust and sea salt. The maximum atmospheric heating occurs over central Africa (due to biomass burning), India and China (due to fossil fuel burning). Figure 3.1 also shows the vertical profile of the atmospheric solar heating rate response in CAM4 STANDARD (other models are similar). Most of the heating occurs near the surface, peaking at ∼925 hPa, and then rapidly decaying to zero near ∼500 hPa. Although aerosol simulations generally reproduce a similar spatial distribution of F_{SFC} and F_{ATM} (not shown), their vertical aerosol heating profile is more uniform, with relatively large heating that extends through the upper-troposphere (Stjern et al., 2017). Based on CAM4 PDRMIP 10xBC simulations, the atmospheric solar heating response remains relatively large up to 100 hPa, with a secondary peak near 200 hPa (Figure 3.1c). Moreover, the lower-tropospheric heating maximum is elevated relative to observationally-constrained fine mode aerosols (∼850 versus 925 hPa). These large differences in the vertical aerosol heating profile imply corresponding differences in the cloud adjustment and aerosol-cloud SDE.

Figure 3.2a shows global ANN mean vertical profiles of the cloud response to observationally-constrained fine mode aerosol forcing without dust and sea salt (STANDARD). Weak increases occur near the surface (especially in CAM4), which then give way to much larger decreases that span the entire troposphere, extending from ∼950 to 250 hPa. Consistently, all models show global annual mean cloud reductions for CLOW, CMED and CHI, with the largest decreases in CLOW and CMED (Table 3.1). The ANN CLOW response varies between −0.43% in GFDL to −0.14% in CAM4. The ANN CMED (CHI) response varies from −0.26% in CAM4 to −0.21% in GFDL (−0.04% in GFDL to −0.12 % in CAM5). Figure 3.2b shows that these cloud responses are consistent with the corresponding change in relative humidity (RH). All three models show weak increases in RH near the surface, which then transitions into larger decreases in RH throughout most of the troposphere. Model agreement on the spatial cloud response exists in several regions. For example, CLOW generally increases over areas with large atmospheric

heating, including Africa and parts of southeast Asia (Figure 3.3 and 3.4). CLOW reductions occur over Indonesia, the Indian Ocean, and parts of the Northern Hemisphere mid- and high-latitudes. Generally similar signed cloud responses occur over both land and ocean, except for high-level cloud—CHI increases over land, but decreases over ocean in all models. The bulk of this CHI increase occurs over central Africa, and is associated with an increase in vertical motion (OMEGA) and convective mass flux (CMF), particularly in the upper-troposphere (Figure 3.5). Although CMF is generally reduced in response to the stabilizing effects of aerosol atmospheric heating—particularly in the lower-troposphere—the large amount of atmospheric heating over Africa (Fig 3.1) acts to destabilize the mid- and upper-troposphere, resulting in rising air and an increase in CHI. To a lesser extent, this is also the case over parts of southeast Asia.

All three models yield an increase in lower-tropospheric stability (S), due to cooling of the surface and warming at 700 hPa (Table 3.2; Figure 3.5). This increase in stability traps moisture near the surface, leading to a corresponding increase in near-surface RH and cloud, including significant increases in cloud (C_{BOT}) and RH (RH_{BOT}) at the model's bottom level. CAM4 yields the largest increase in C_{BOT} (Table 3.1), which is consistent with its S-based marine stratocumulus parameterization. However, above the near-surface, decreases in lower-tropospheric RH are consistent with an overall decrease in CLOW. For example, $RH_{925-700}$ decreases between −0.19 to −0.37% in GFDL and CAM4, respectively (Table 3.2). Similarly, decreases in mid- and upper-tropospheric RH are consistent with decreases in CMED and CHI. $RH_{600-500}$ decreases between −0.09 to −0.25% in GFDL and CAM4; $RH_{300-250}$ decreases between −0.01 and −0.22% in GFDL and CAM5, respectively. A more detailed regression analysis (Table 3.3) shows that RH is generally the best predictor, with S (OMEGA) also important for the CLOW (CMED and CHI) response (Figure 3.6). Thus, observationally-constrained aerosol forcing yields overall cloud reductions, most of which is driven by decreases in RH and subsequent cloud burn-off.

The vertical profile of simulated climatological clouds differs in our models (Figure 3.7). For example, CAM5 shows the largest amount of cloud throughout the atmospheric column; GFDL shows the least amount of low-level cloud; and CAM4 shows the least amount of mid-level cloud. However, there does not seem to be a clear connection between the cloud response,

and the amount of climatological cloud, implying parameterization differences (Methods) likely drive the bulk of any contrasting cloud responses in these models.

Figure 3.8 shows the aerosol-cloud SDE (Methods) for all three models. All models yield a positive global annual mean SDE. The largest SDE occurs in GFDL at 0.52 W m^{-2}, followed by CAM5 and CAM4 at 0.30 and 0.29 W m^{-2}, respectively (Table 3.1). Several regions of SDE model agreement exist, including the Indian Ocean, most of south America, and parts of the NH mid-latitudes (Figure 3.9). Moreover, the SDE is dominated by shortwave effects, which drives the positive SDE; longwave effects act to mute the positive SDE. These changes are consistent with the corresponding changes in clouds. Low clouds tend to have a net cooling effect on the planet, due to high albedo; high clouds tend to have a net warming effect, due to their greenhouse effect. Mid-level clouds are a combination of both, but we find they tend to affect the SDE similarly to low-level clouds. Thus, the decrease in low and mid-level cloud drives the positive SDE (in the shortwave), and the decrease in high-level clouds weakens this through enhanced longwave cooling. We also note that the rapid adjustments are positive in all models (Table 3.1), and dominated by the aerosol-cloud SDE. Although changes in temperature and moisture also contribute to the rapid adjustments, and generally enhance the warming, this contribution is smaller than that due to cloud adjustments.

Several recent studies have shown the rapid adjustments to absorbing aerosol are negativeStjern et al. (2017). PDRMIP 10xBC aerosol simulations yield a multi-model mean rapid adjustment of −0.88, ranging from −0.44 to −1.48 W m^{-2}, similar to previously published valuesStjern et al. (2017). Additional analyses reveals that the rapid adjustment is dominated by the longwave component, with a multi-model mean of −1.14, ranging from −0.45 to −2.24 W m^{-2} (Table 3.4). The corresponding multi-model mean shortwave component is 0.25 (−0.21 to 0.76) W m^{-2}. The importance of longwave radiation to the rapid adjustment is consistent with the corresponding cloud changes (Figure 3.2c), including increases in CLOW (0.06; 0.02 to 0.11%), decreases in CMED (−0.17; −0.49 to 0.02%), and relatively large decreases in CHI (−0.37; −0.79 to −0.09%). The decrease in CMED is consistent with the weakly positive RAP_{ADJ-SW}, and the large decrease in CHI is consistent with the negtative RAP_{ADJ-LW}. Fur-

thermore, PDRMIP cloud responses are consistent with the corresponding RH change (Figure 3.2d). Although PDRMIP models show smaller decreases in CHI over land (including increases over Africa and parts of India/southeast Asia), as compared to ocean, CHI decreases over both ocean and land.

Unfortunately, PDRMIP did not archive the relevant diagnostics to quantify the relative importance of the aerosol-cloud SDE to the rapid adjustment. Calculation of the shortwave cloud forcing due to absorbing aerosol using standard techniques leads to a positive bias (in the shortwave), by increasing the radiative warming when the absorbing aerosol lies above clouds (Ghan, 2013). Thus, it is necessary to use the clear sky cloud radiative forcing, and only CAM4-PDRMIP archived this diagnostic. CAM4-PDRMIP yields an aerosol-cloud SDE of -1.05 W m^{-2}, broken down into -0.28 W m^{-2} in the shortwave and -0.77 W m^{-2} in the longwave (Table 3.1). Thus, the aerosol-cloud SDE is a relatively large negative number, dominated by longwave radiation. This is consistent with the aforementioned cloud changes, and in particular, the large decrease in CHI (Table 3.4). This result also shows that the rapid adjustment is dominated by aerosol-cloud SDEs, as opposed to changes in temperature and moisture. This “residual term" (Methods) is -0.29 W m^{-2}, decomposed into 0.07 W m^{-2} in the shortwave and -0.36 W m^{-2} in the longwave. These changes are consistent with enhanced water vapor leading to more solar absorption (positive shortwave residual) and atmospheric warming leading to enhanced longwave cooling (negative longwave residual). Although the aerosol-cloud SDE cannot be quantified in the other PDRMIP models, the cloud changes are qualitatively similar to those in CAM4-PDRMIP, implying similar results for the aerosol-cloud SDE.

To test the hypothesis that the cause of the SDE sign difference using observationally-constrained aerosols, relative to PDRMIP and other aerosol simulations, is related to the vertical aerosol heating profile (Figure 3.1), we perform sensitivity simulations with observationally-constrained aerosol forcing, but we apply it uniformly in the vertical (“VERTUNIF" simulations). Figure 3.2 shows that VERTUNIF yields very different results relative to STANDARD, and moreover, VERTUNIF yields cloud changes very similar to PDRMIP. Relatively large increases in cloud and RH occur near the surface, extending up to $\sim$800 hPa. Above $\sim$800 hPa, decreases in both cloud

and RH exist, with relatively large reductions above ∼300 hPa. Consistently, VERTUNIF yields increases in CLOW, decreases in CMED, and large decreases in CHI (Table 3.1, Figure 3.10). Several regions of cloud response model agreement exist, particularly for CHI (Figure 3.4). These changes are again consistent with ΔRH. Relative to STANDARD, VERTUNIF $RH_{925-700}$ now increases and $RH_{300-250}$ yields larger and more consistent decreases (Table 3.2; Figure 3.11). In turn, the effective radiative forcing (ERF) swaps sign from positive to negative, as does the rapid adjustment and the aerosol cloud SDE (which still dominates the rapid adjustment). GFDL VERTUNIF yields an aerosol-cloud SDE of −0.41 m^{-2}, which increases to −0.67 m^{-2} in CAM4 (Figure 3.8). Moreover, the SDE is now dominated by longwave effects (cooling), consistent with the large decrease in high-level cloud. These results are also qualitatively consistent with other studies (Hodnebrog et al., 2014; Samset and Myhre, 2015) that found weaker decreases in CHI and a less negative SDE when BC above 200 and 500 hPa was restricted.

We quantified the roles of three predictors of simulated cloud—S ($\theta_{700} - \theta_{sfc}$), RH and vertical motion (OMEGA, the vertical component of velocity in pressure coordinates)—using regression models applied to the control simulation. Models are independently fit to land and ocean data for the tropics (30S-30N), Northern Hemisphere extratropics (NHE; 30-90N), and the Southern Hemisphere extratropics (SHE; 30-90S). Generally, RH is the best predictor of the cloud response, but S is also important for CLOW, and OMEGA is important for CMED and CHI. Below is a summary of the results, based on GFDL AM2.1. Similar results are obtained with CAM4/5.

For CHI, the model based on RH (at 300 hPa) yields coefficient of determination (R^2) values that range from 0.38 (NHE ocean) to 0.83 (tropical land) (Table 3.3). Similarly, the R^2 of the model based on OMEGA (at 300 hPa) ranges from 0.26 (SHE land) to 0.70 (tropical ocean). The R^2 of the bivariate RH+OMEGA model ranges from 0.54 (NHE land) to 0.87 (tropical land). Moreover, this bivariate regression model predicts fairly well the change in mean CHI, given the changes in mean RH and OMEGA, including the land/sea contrast in the tropics. The predicted (actual) changes are −0.11 (−0.18) over tropical land and 0.52 (0.76) over tropical oceans (Figure 3.6). The corresponding global values are −0.01 and −0.04, respectively.

For CMED, RH (at 600 hPa) is again the best predictor, followed by OMEGA (at 600 hPa) especially over the tropical and SHE oceans. The best model uses both OMEGA and RH (at 600 hPa), yielding a R^2 that ranges from 0.35 (tropical ocean) to 0.88 (SHE ocean). Globally, the predicted (actual) changes are -0.15 (-0.21). For CLOW, $RH_{925-700}$ yields R^2 values ranging from 0.52 (tropical ocean) to 0.73 (NHE land). S is also important over land, particularly NHE land ($R^2 = 0.39$). The best model uses $RH_{925-700}$ over the ocean, and $RH_{925-700}$ and S over land, resulting in a global mean predicted CLOW of -0.23, relative to the simulated decrease of -0.43.

These results show that the aerosol-cloud SDE can mostly be explained by changes in stability and relative humidity for low-level clouds, and vertical motion and relative humidity for mid- and high-level clouds.

The cloud response differences between VERTUNIF and STANDARD are consistent with the importance of RH changes, and the location of the aerosol heating. VERTUNIF yields similar changes in S, but this is due to stronger surface cooling, and weaker warming at 700 hPa (Table 3.2). Both are consistent with the altered vertical heating profile. Similar to STANDARD, the increase in S leads to an increase in RH_{BOT} and C_{BOT}. This is particularly prominent over southeast Asia in GFDL, where large increases in S and RH_{BOT} occur (Figure 3.10 and 3.11). However, lower-tropospheric RH also increases ($RH_{925-700}$ increases by 0.05 to 0.12%), in contrast to STANDARD. This is consistent with an increase in CLOW. Mid- and upper-tropospheric RH also decrease in VERTUNIF, with much larger decreases in upper-tropospheric RH than in STANDARD ($\Delta RH_{300-250}$ is -0.11 to -0.46% versus -0.01 to -0.22%, respectively). This is consistent with decreases in CMED, and in particular, CHI. Thus, with less VERTUNIF atmospheric heating in the lower-troposphere, but similar increases in stability, the increase in S and associated moisture trapping and RH increase dominates the burn-off of low-level cloud, leading to an increase in CLOW. Similarly, with more atmospheric heating in the upper-troposphere in VERTUNIF, there is more burn-off of high-level clouds, leading to a decrease in CHI. Furthermore, CHI does not increase over land, including the large local increase over Africa. A more vertically uniform heating profile does not lead to atmospheric destabilization over Africa, as in

STANDARD. Thus, a decrease in CHI over ocean and land in VERTUNIF also leads to a larger global mean decreases in CHI. This argument can also be extended to PDRMIP 10xBC simulations.

3.4 Conclusions

Using observationally-constrained fine-mode aerosol forcing, we find a robust positive aerosol-cloud SDE, that acts to warm the climate system. This response is consistent with the corresponding cloud changes, including relatively large decreases in CLOW and CMED. Aerosol simulations, however, yield the opposite response—a negative SDE, primarily due to large decreases in CHI and enhanced longwave cooling. These differences are related to the vertical profile of aerosol atmospheric heating, with aerosol simulations yielding a relatively vertically uniform profile, with strong heating that extends up to 100hPa. The negative SDE and the corresponding cloud changes are qualitatively reproduced with a simple idealized simulation forced with observationally-constrained aerosols, but with vertically uniform atmospheric heating. We note that our approach has uncertainties of its own, including the observationally-constrained aerosol forcing, lack of consistency between the aerosol forcing and simulated meteorology, as well as the simulated cloud fields. Furthermore, global models may not be able to simulate sub-grid scale features (e.g., cloud layer thickness, cloud-top entrainment) which may influence the SDE. However, they should adequately simulate the large-scale features important for the SDE, including changes in stability and RH, and modification of the large-scale atmospheric circulation. Thus, our results imply aerosol simulations lead to a negatively biased SDE. We also suggest that this bias may translate into other aspects of the response, including surface temperature and precipitation.

Table 3.1: Global annual mean cloud changes and top-of-the-atmosphere radiative effects. Responses are shown for observationally constrained fine-mode aerosol forcing without dust and sea salt (STANDARD), analogous simulations with vertically uniform aerosol atmospheric heating (VERTUNIF) and CAM4-PDRMIP. Cloud changes are shown for the model's lowest level (C_{BOT}), as well as low-level (CLOW); mid-level (CMED); and high-level (CHI). Radiative effects include the effective radiative forcing (ERF); rapid adjustments (RAP_{ADJ}) and the aerosol-cloud semi-direct effect (SDE), which is also decomposed into shortwave (SDE_{SW}) and longwave (SDE_{LW}) components. RAP_{ADJ} is calculated as ERF−IRF, where IRF is the instantaneous radiative forcing (−0.11 W m^{-2} for observationally-constrained fine-mode aerosol without dust and sea salt). All changes are significant at the 90% confidence level, unless denoted by bold font. Cloud change units are %; ERF, RAP_{ADJ} and SDE units are W m^{-2}.

				STANDARD					
Model	C_{BOT}	CLOW	CMED	CHI	ERF	RAP_{ADJ}	SDE	SDE_{SW}	SDE_{LW}
CAM4	0.33	−0.14	−0.26	−0.07	0.32	0.43	0.29	0.46	−0.17
CAM5	0.07	−0.26	−0.22	−0.12	0.29	0.40	0.30	0.40	−0.10
GFDL	**0.05**	−0.43	−0.21	**−0.04**	0.43	0.54	0.52	0.67	−0.15
				VERTUNIF					
CAM4	0.10	0.25	−0.19	−0.54	−0.61	−0.50	−0.67	−0.17	−0.50
CAM5	0.09	0.21	−0.22	−0.80	−0.49	−0.38	−0.54	**0.07**	−0.61
GFDL	0.11	0.18	−0.20	−0.71	−0.56	−0.45	−0.41	0.21	−0.62
				PDRMIP					
CAM4-PDRMIP	0.40	0.11	−0.19	−0.30	0.76	−1.34	−1.05	−0.28	−0.77

Table 3.2: Global annual mean changes in temperature and relative humidity. Responses are shown for observationally constrained fine-mode aerosol forcing without dust and sea salt (STANDARD) and analogous simulations with vertically uniform aerosol atmospheric heating (VERTUNIF) for surface temperature (T_{sfc}), 700 hPa temperature (T_{700}), lower-tropospheric stability ($S = \theta_{700} - \theta_{sfc}$), relative humidity at the model's bottom level (RH_{BOT}), lower-troposphere ($RH_{925-700}$), mid-troposphere ($RH_{600-500}$) and upper-troposphere ($RH_{300-250}$). All changes are significant at the 90% confidence level, unless denoted by bold font. Temperature and stability units are K; RH units are %.

				STANDARD			
Model	T_{sfc}	T_{700}	S	RH_{BOT}	$RH_{925-700}$	$RH_{600-500}$	$RH_{300-250}$
CAM4	**0.001**	0.13	0.14	0.35	−0.37	−0.25	−0.19
CAM5	**0.01**	0.16	0.17	0.28	−0.27	−0.22	−0.22
GFDL	−0.09	0.09	0.19	0.17	−0.19	−0.09	**−0.01**
				VERTUNIF			
CAM4	−0.10	0.04	0.15	0.33	0.11	−0.15	−0.23
CAM5	−0.06	0.08	0.15	0.28	0.12	−0.10	−0.46
GFDL	−0.12	0.12	0.26	0.30	**0.05**	**−0.01**	−0.11

Table 3.3: Coefficient of determination (R^2) of cloud regression models. Models are independently fit to GFDL AM2.1 land and ocean data for the tropics (30S-30N), Northern Hemisphere extratropics (NHE; 30-90N), and the Southern Hemisphere extratropics (SHE; 30-90S) for low-level (CLOW); mid-level (CMED); and high-level (CHI) cloud. Predictors include relative humidity (RH), lower-tropospheric stability ($S = \theta_{700} - \theta_{sfc}$), and vertical velocity (OMEGA).

		CLOW		
Region	$RH_{925-700}$	S	$OMEGA_{850}$	$RH_{925-700}$+S
NHE Land	0.73	0.39	0.01	0.79
NHE Ocean	0.60	0.11	0.07	0.68
Tropics Land	0.56	0.14	0.03	0.59
Tropics Ocean	0.52	0.17	0.03	0.60
SHE Land	0.72	0.09	0.001	0.76
SHE Ocean	0.67	0.0002	0.20	0.69
		CMED		
Region	RH_{600}	S	$OMEGA_{600}$	RH_{600}+$OMEGA_{600}$
NHE Land	0.76	0.10	0.19	0.78
NHE Ocean	0.67	0.03	0.39	0.72
Tropics Land	0.52	0.0001	0.26	0.53
Tropics Ocean	0.29	0.14	0.37	0.35
SHE Land	0.82	0.02	0.04	0.82
SHE Ocean	0.87	0.002	0.52	0.88
		CHI		
Region	RH_{300}	S	$OMEGA_{300}$	RH_{300}+$OMEGA_{300}$
NHE Land	0.45	0.03	0.28	0.54
NHE Ocean	0.38	0.02	0.36	0.63
Tropics Land	0.83	0.08	0.69	0.87
Tropics Ocean	0.78	0.15	0.70	0.83
SHE Land	0.44	0.07	0.26	0.56
SHE Ocean	0.55	0.02	0.49	0.67

Table 3.4: Global annual mean cloud and top-of-the-atmosphere radiative responses in PDRMIP 10xBC simulations. Cloud changes include low-level (CLOW); mid-level (CMED); and high-level (CHI) cloud. Radiative effects include the instantaneous radiative forcing (IRF; shortwave radiation only), effective radiative forcing (ERF) and rapid adjustments (RAP_{ADJ}). ERF and RAP_{ADJ} are also decomposed into shortwave (SW) and longwave (LW) components. RAP_{ADJ-SW} is calculated as $ERF_{SW}-IRF$; RAP_{ADJ-LW} equals ERF_{LW}. In the case of IPSL-CM5A, which includes aerosol-cloud interactions (IRF_{aci} is -0.07 W m^{-2}), the RAP_{ADJ-SW} is calculated as $ERF_{SW}-IRF-IRF_{aci}$. Cloud changes are calculated as a vertical average (1000 to 680 hPa for CLOW; 680 to 440 hPa for CMED; 440 to 50 hPa for CHI). Responses are significant at the 90% confidence level, unless denoted by bold font. Cloud change units are %; IRF, ERF, and RAP_{ADJ} units are W m^{-2}. Only those PDRMIP models that archived IRF are included.

Model	CLOW	CMED	CHI	IRF	ERF	ERF_{SW}	ERF_{LW}	RAP_{ADJ}	RAP_{ADJ-SW}
CESM-CAM4	0.11	−0.19	−0.30	2.10	0.76	1.89	−1.13	−1.34	−0.21
GISS-E2-R	0.06	**0.02**	−0.28	1.88	1.25	1.91	−0.66	−0.63	0.03
HadGEM2-ES	**0.02**	−0.49	−0.41	3.29	2.85	4.05	−1.20	−0.44	0.76
MIROC-SPRINTARS	0.05	−0.10	−0.09	1.22	0.67	1.12	−0.45	−0.55	−0.10
IPSL-CM5A	0.07	−0.09	−0.79	2.33	0.78	3.02	−2.24	−1.48	0.76

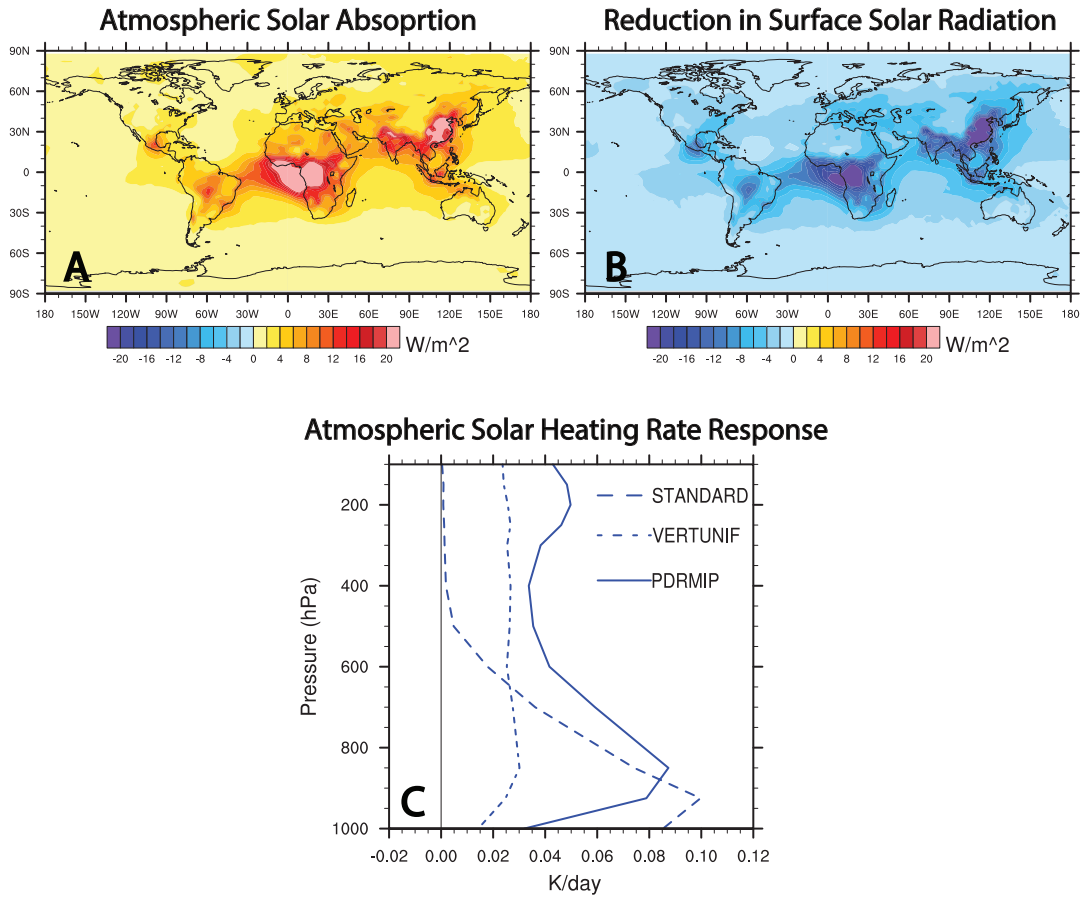

Figure 3.1: Annual mean observationally-constrained fine mode aerosol forcing without dust and sea salt. Spatial maps of (A) atmospheric solar absorption and (B) reduction in surface solar radiation. (C) Global mean vertical profile of the corresponding atmospheric solar heating rate response in CAM4 with observationally-constrained fine mode aerosol forcing without dust and sea salt (STANDARD). Also included is the corresponding heating rate response in CAM4 with the same observationally-constrained fine mode aerosol forcing, but with vertically uniform aerosol atmospheric heating (VERTUNIF); and CAM4-PDRMIP 10xBC simulations. Units are W m^{-2} for (A, B) and K day^{-1} for (C).

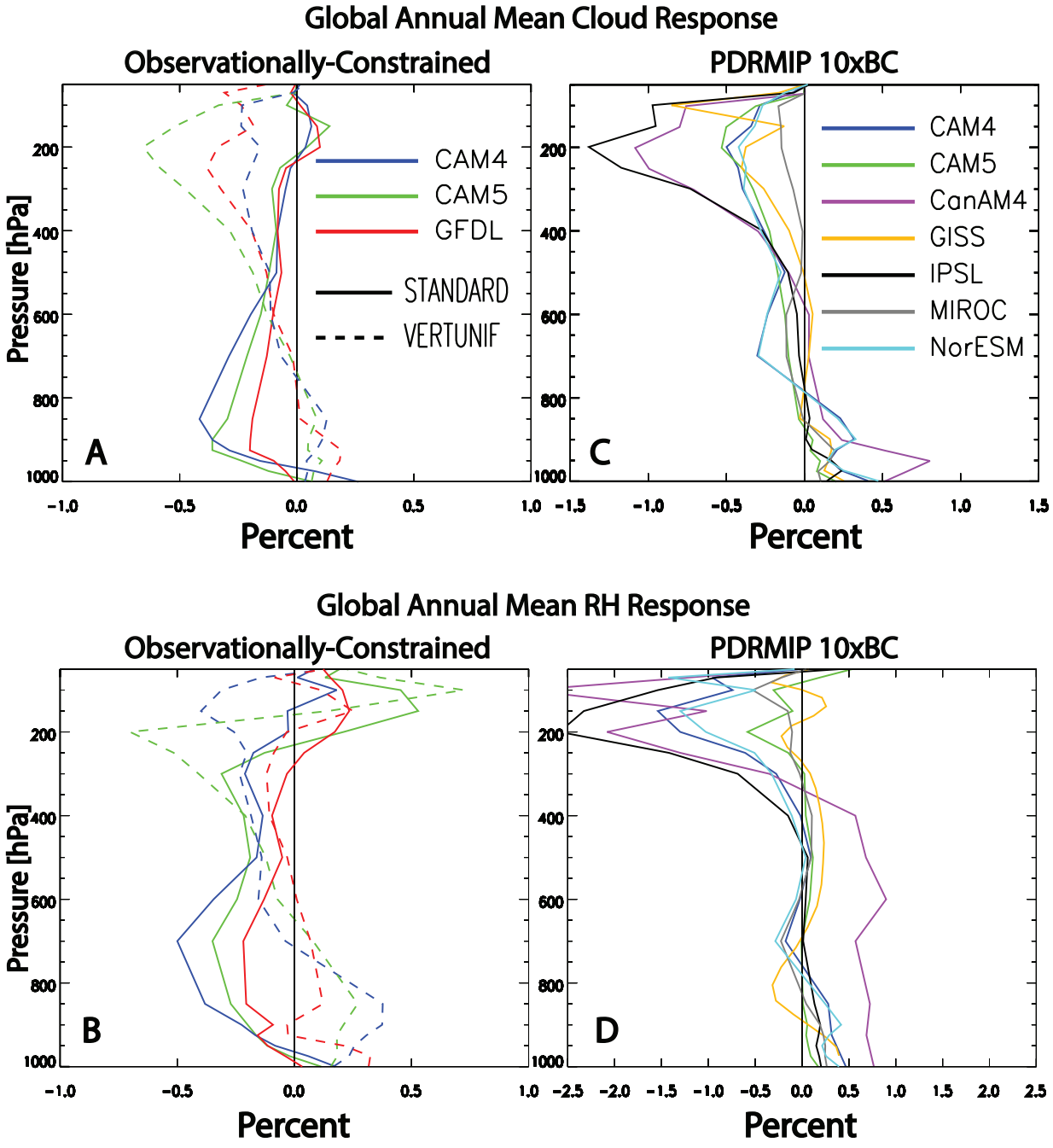

Figure 3.2: Global annual mean vertical profiles of the cloud and relative humidity response. (A, C) Cloud and (B, D) relative humidity (RH) for (left panels) CAM4, CAM5 and GFDL AM2.1 forced with observationally constrained fine-mode aerosol forcing without dust and sea salt (STANDARD; solid); analogous simulations with vertically-uniform aerosol atmospheric heating (VERTUNIF; dashed); and (right panels) PDRMIP 10xBC simulations. Units are %.

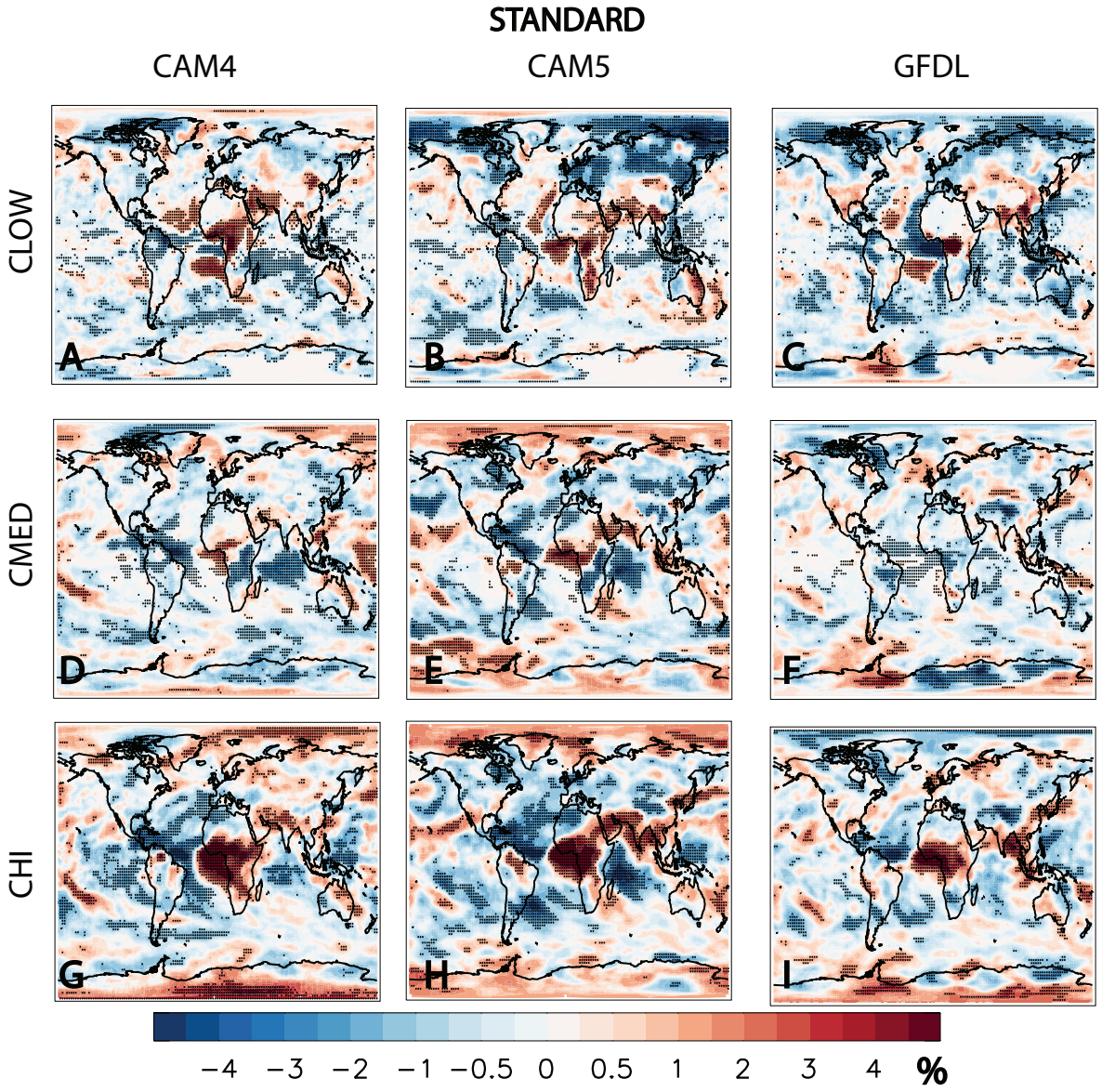

Figure 3.3: Annual mean cloud response to observationally constrained fine-mode aerosol forcing without dust and sea salt. (A-C) Low-level (CLOW); (D-F) mid-level (CMED); and (G-I) high-level (CHI) cloud response for (left panels) CAM4; (center panels) CAM5; and (right panels) GFDL AM2.1. Symbols denote significance at the 90% confidence level. Units are %.

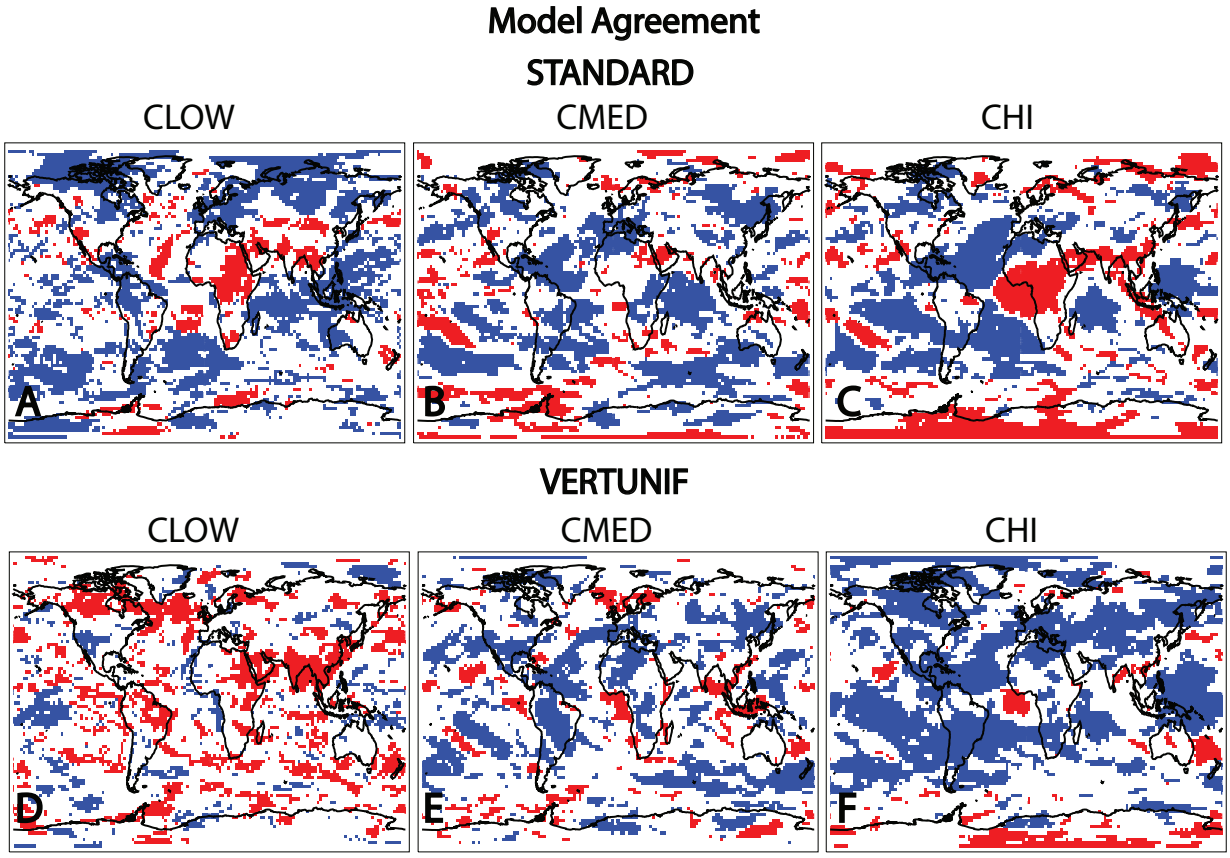

Figure 3.4: Cloud response model agreement. (A-C) Observationally-constrained fine-mode aerosols without dust and sea salt (STANDARD); (D-F) analogous simulations with vertically uniform aerosol atmospheric heating (VERTUNIF) for (left panels) CLOW; (middle panels) CMED; and (right panels) CHI. Regions where all three models agree on a cloud increase (decrease) are colored red (blue).

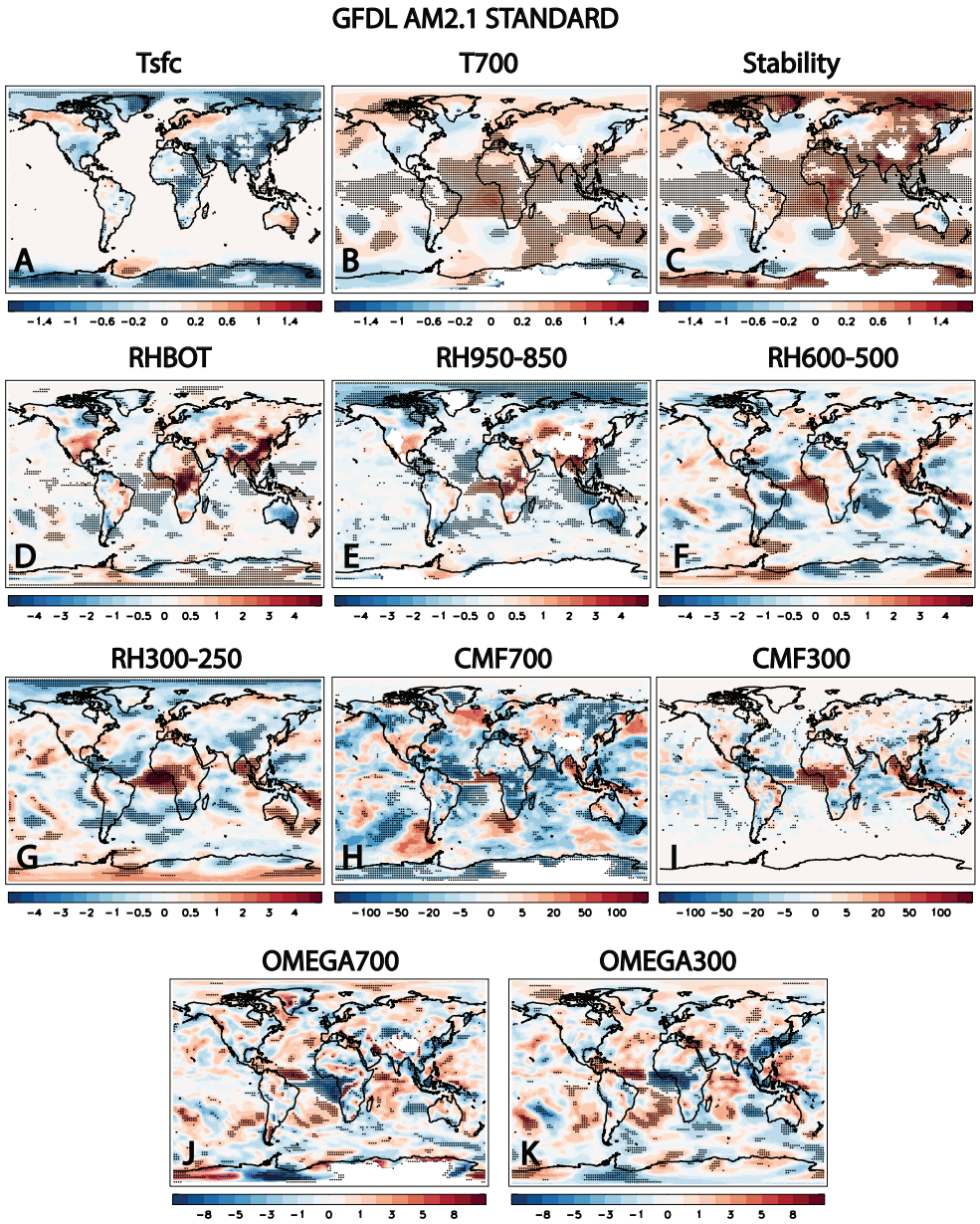

Figure 3.5: GFDL AM2.1 annual mean climate response to observationally constrained fine-mode aerosol forcing without dust and sea salt. (A) Surface temperature (T_{sfc}); (B) 700 hPa temperature (T_{700}); (C) lower-tropospheric stability ($S = \theta_{700} - \theta_{sfc}$); (D) relative humidity at the model's bottom level (RH_{BOT}); (E) lower-troposphere RH ($RH_{925-700}$); (F) mid-troposphere RH ($RH_{600-500}$); (G) upper-troposphere RH ($RH_{300-250}$); (H) 700 hPa convective mass flux (CMF_{700}); (I) 300 hPa convective mass flux (CMF_{300}); (J) 700 hPa pressure vertical velocity (OMEGA700); and 300 hPa pressure vertical velocity (OMEGA300) Symbols denote significance at the 90% confidence level. Temperature and stability units are K; RH units are %; OMEGA units are hPa day^{-1} and CMF units are kg m^{-2} day^{-1}. Rising (sinking) air is associated with − (+) OMEGA.

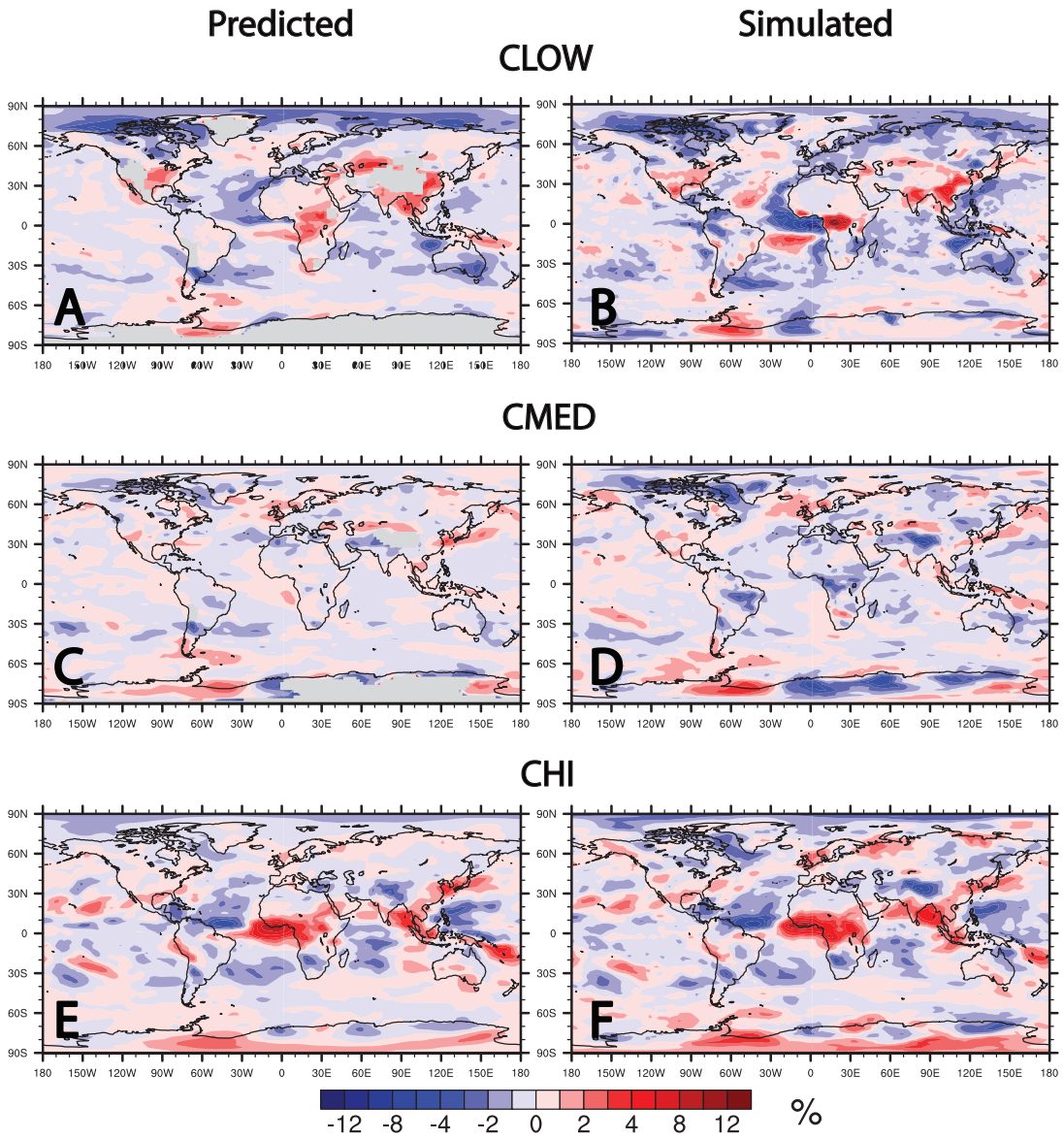

Figure 3.6: Predicted and simulated cloud responses in GFDL AM2.1. Predicted (left panels) and simulated (right panels) responses for (A-B) low-level (CLOW); (C-D) mid-level (CMED); and (E-F) high-level (CHI) cloud. Predicted cloud responses are based on bivariate regression models, including $RH_{925-700}$ and S for CLOW; RH_{600} and $OMEGA_{600}$ for CMED; and RH_{300} and $OMEGA_{300}$ for CHI. Units are %.

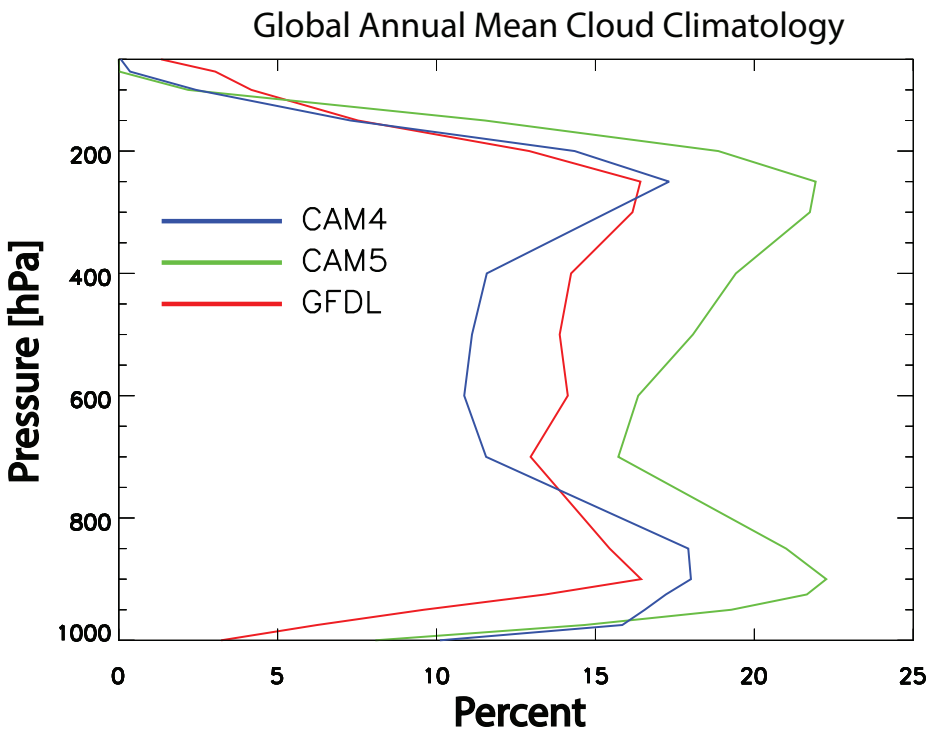

Figure 3.7: Global annual mean vertical profiles of cloud climatology. Cloud climatologies are shown for CAM4, CAM5 and GFDL AM2.1. Units are %.

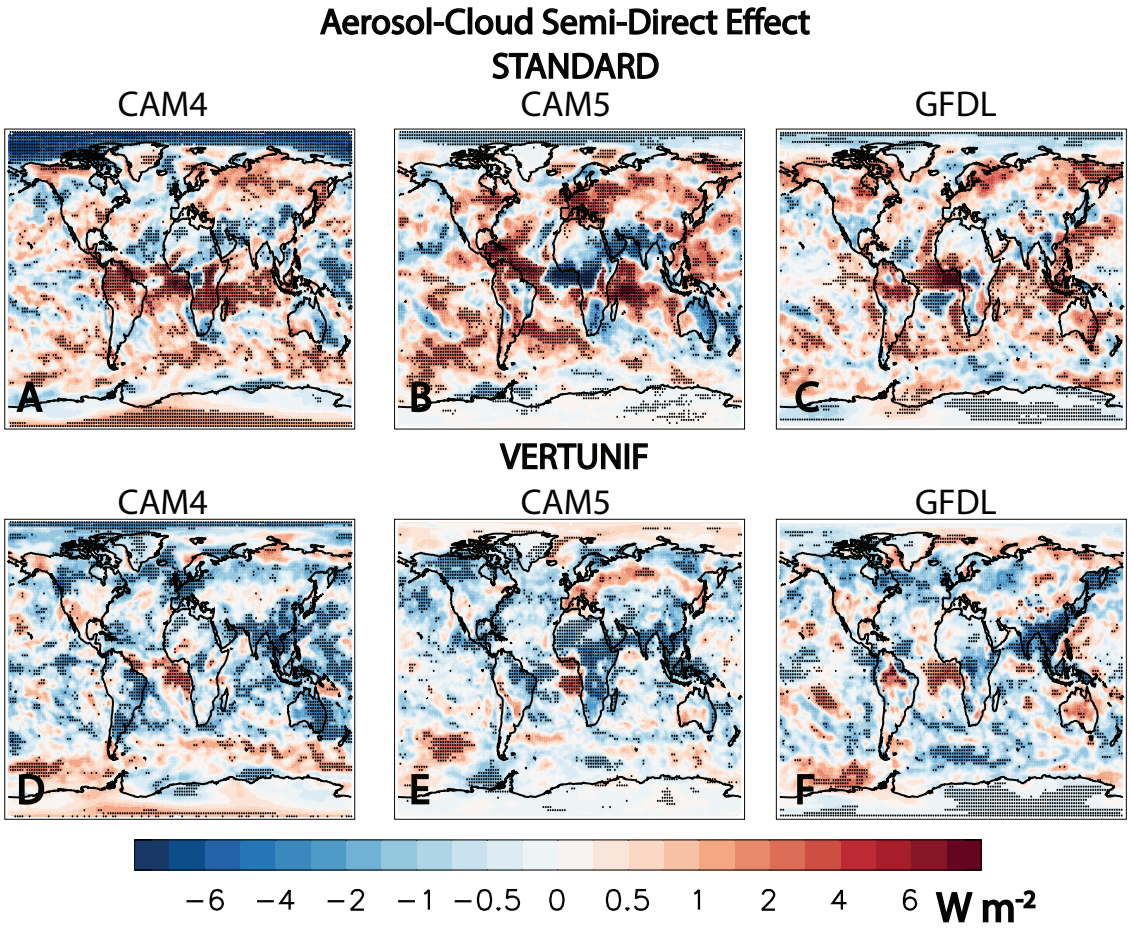

Figure 3.8: Annual mean aerosol-cloud semi-direct effect. Semi-direct effect (SDE) based on (A-C) observationally constrained fine-mode aerosol forcing without dust and sea salt (STANDARD); (D-F) analogous simulations with vertically uniform aerosol atmospheric heating (VERTUNIF) for CAM4, CAM5 and GFDL AM2.1. Symbols denote significance at the 90% confidence level. Units are W m^{-2}.

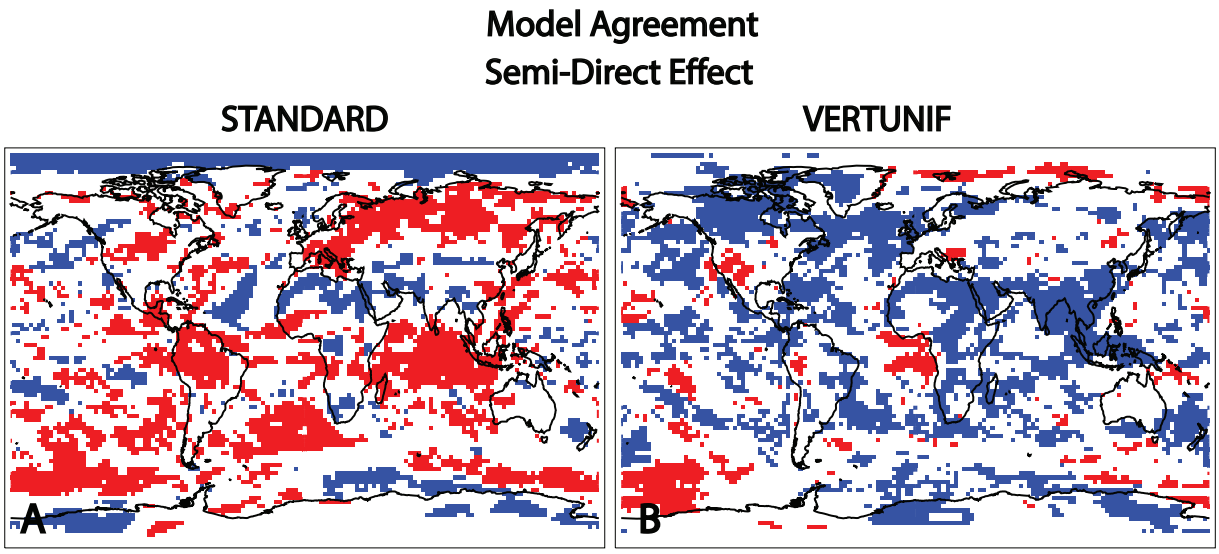

Figure 3.9: Aerosol-cloud semi-direct effect model agreement. (A) Observationally-constrained fine-mode aerosols without dust and sea salt (STANDARD); (B) analogous simulations with vertically uniform aerosol atmospheric heating (VERTUNIF). Regions where all three models agree on positive (negative) SDE are colored red (blue).

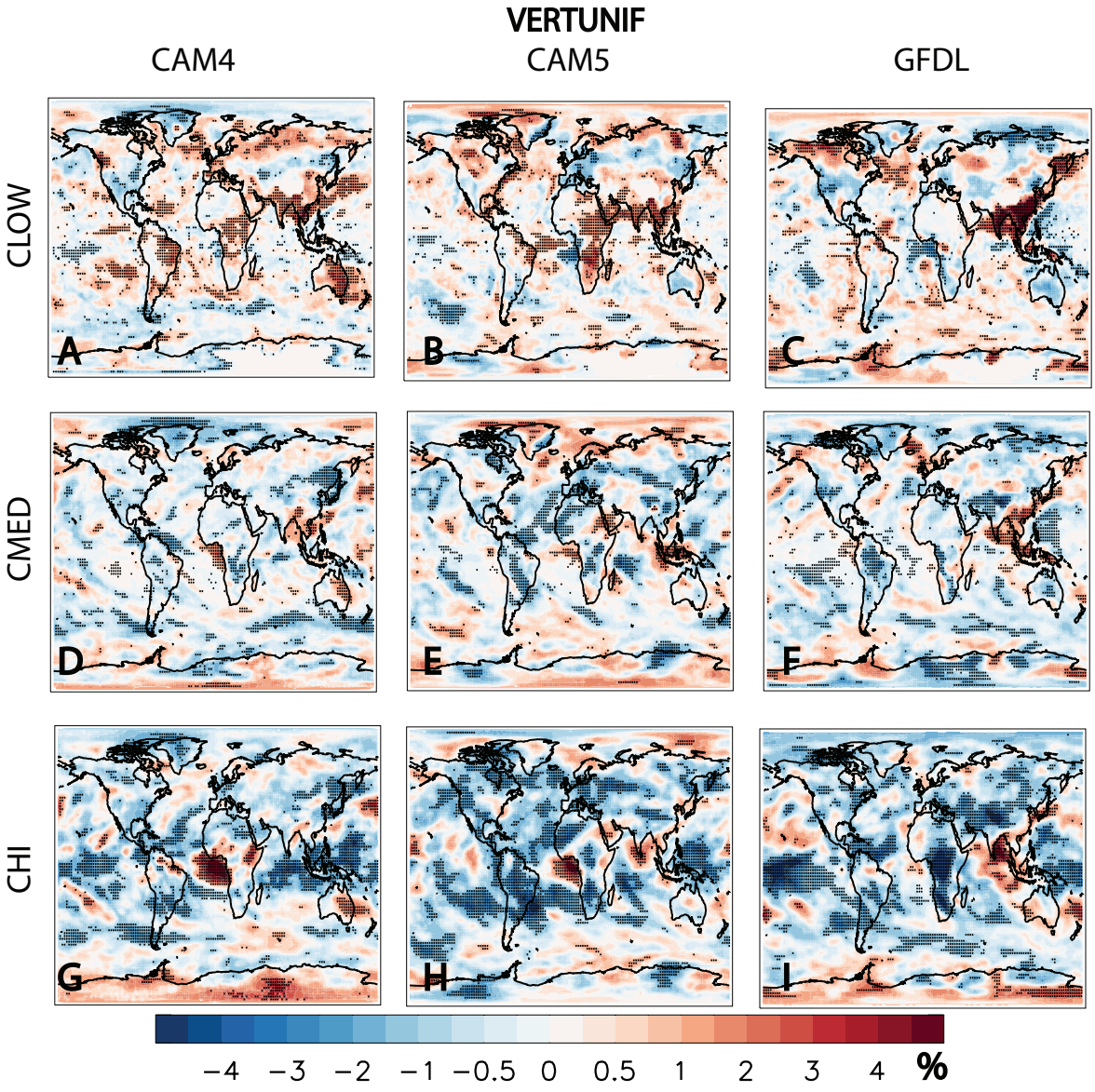

Figure 3.10: Annual mean cloud response to observationally constrained fine-mode aerosol forcing with vertically uniform aerosol atmospheric heating. (A-C) Low-level (CLOW); (D-F) mid-level (CMED); and (G-I) high-level (CHI) cloud response for (left panels) CAM4; (center panels) CAM5; and (right panels) GFDL AM2.1. Symbols denote significance at the 90% confidence level. Units are %.

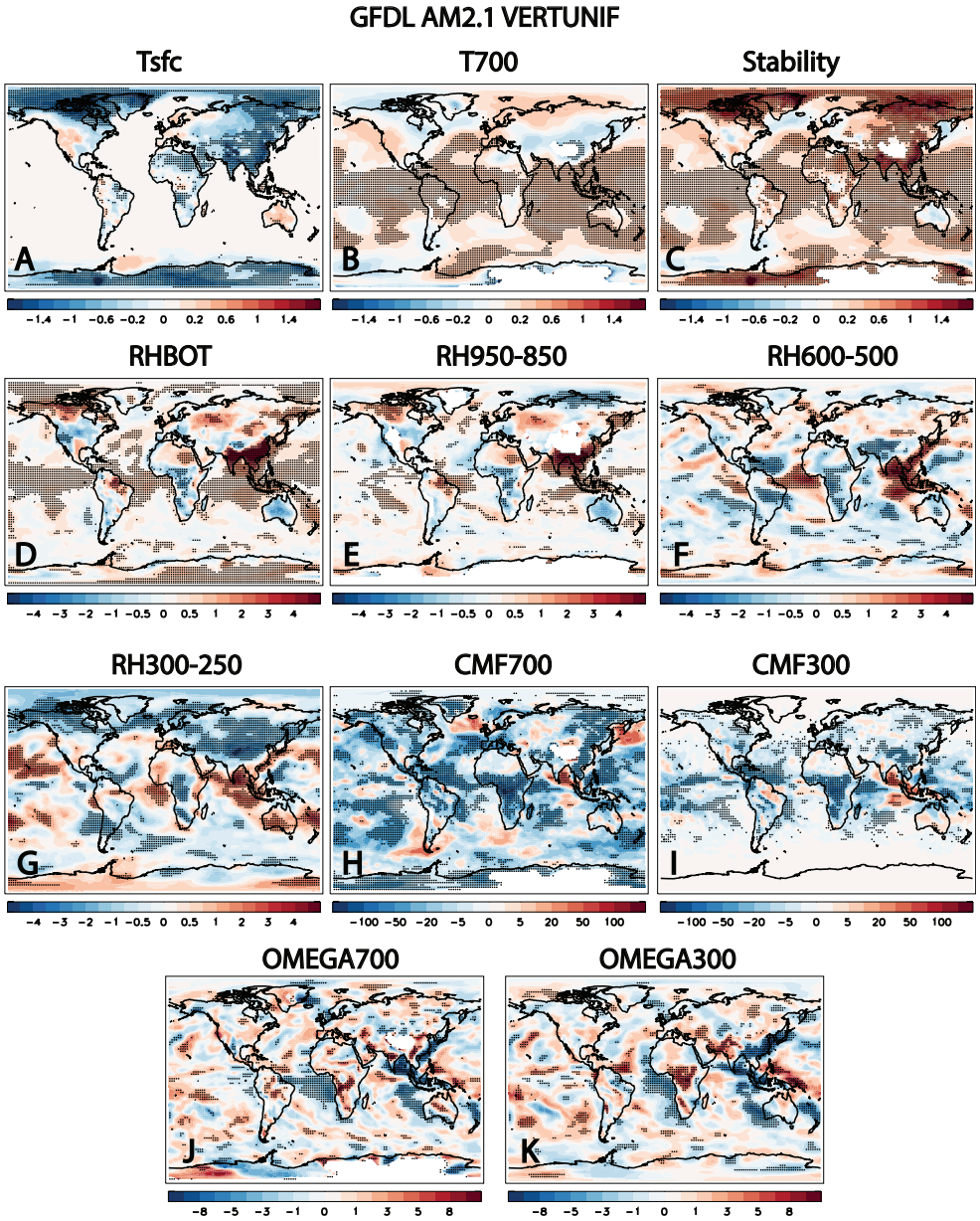

Figure 3.11: GFDL AM2.1 annual mean climate response to observationally constrained fine-mode aerosol forcing with vertically uniform aerosol atmospheric heating. (A) Surface temperature (T_{sfc}); (B) 700 hPa temperature (T_{700}); (C) lower-tropospheric stability ($S = \theta_{700} - \theta_{sfc}$); (D) relative humidity at the model's bottom level (RH_{BOT}); (E) lower-troposophere RH ($RH_{925-700}$); (F) mid-troposphere RH ($RH_{600-500}$); (G) upper-troposphere RH ($RH_{300-250}$); (H) 700 hPa convective mass flux (CMF_{700}); (I) 300 hPa convective mass flux (CMF_{300}); (J) 700 hPa pressure vertical velocity (OMEGA700); and 300 hPa pressure vertical velocity (OMEGA300). Symbols denote significance at the 90% confidence level. Temperature and stability units are K; RH units are %; OMEGA units are hPa day^{-1} and CMF units are kg m^{-2} day^{-1}. Rising (sinking) air is associated with − (+) OMEGA.

Chapter 4

Summary and Conclusions

4.1 Chapter 2: Impact of Saharan dust on North Atlantic marine stratocumulus clouds: Importance of the semi-direct effect

To estimate the aerosol-cloud radiative effect of Saharan dust on North Atlantic MSc , we use observational data from multiple sensors in the NASA A-Train satellite constellation from 2004 to 2012. The aerosol-cloud radiative effect is estimated using two different methods, following Quaas et al. (2008) (Method 1) and Chen et al. (2014) (Method 2). The annual mean aerosol cloud radiative effect estimated by Method 1 is -1.5 ± 1.4 Wm^{-2}. Estimating the radiative effect using Method 2 yields similar results, with an annual mean of -1.5 ± 1.6 Wm^{-2}. Thus, Saharan dust modifies MSc in a way that acts to cool the planet. There is a strong seasonal variation, with the aerosol-cloud radiative effect switching from significantly negative during the boreal summer to weakly positive during boreal winter. Both methods also yield a seasonal maximum negative radiative effect during summer, which is consistent with more Saharan dust and MSc during summer. Furthermore, both methods yield a reversal in the sign of the aerosol cloud radiative effect, which switches from negative to positive during the winter season. When most dust resides above the clouds during summer, aerosol-cloud microphysical effects that involve the co-location of aerosol and cloud, such as the second aerosol indirect effect (CLE), would likely be muted relative to the SDE. Moreover, the positive value of the aerosol-cloud radiative

effect during winter, when most dust resides within MSc, indicates that the SDE is dominant—that is the only mechanism by a negative aerosol-cloud radiative effect can be obtained. We conclude that aerosol-cloud radiative effects associated with Saharan dust and North Atlantic MSc are dominated by the semi-direct effect.

4.2 Chapter3: Aerosol-cloud semi-direct effects enhance warming of the climate system

We investigate the SDE using multiple models driven by observationally constrained fine-mode aerosol forcing without dust and sea salt (Chung et al., 2016). We find a significant global annual mean decrease in low and mid-level clouds, and weaker decreases in high-level clouds, which leads to a positive SDE dominated by shortwave radiation. Aerosol simulations, however, yield the opposite response—a negative SDE, primarily due to large decreases in CHI and enhanced longwave cooling. Unlike aerosol simulations, which yield a relatively vertically uniform aerosol atmospheric heating profile with significant upper-tropospheric heating, observation-based heating peaks in the lower-troposphere and then decays to zero in the mid-troposphere. The negative SDE and the corresponding cloud changes are qualitatively reproduced with a simple idealized simulation forced with observationally-constrained aerosols, but with vertically uniform atmospheric heating. Our results therefore suggest that model simulations lead to a negatively biased SDE, due to an aerosol atmospheric heating profile that is too vertically uniform with strong heating that extends up to 100hPa. We also suggest that this bias may affect other aspects of the response, including surface temperature and precipitation.

References

Ackerman, A. S., Toon, O. B., Stevens, D. E., Heymsfield, A. J., Ramanathan, V., and Welton, E. J.: 2000, *Science* **288**, 1042

Ackerman, A. S., Toon, O. B., Taylor, J. P., Johnson, D. W., Hobbs, P. V., and Ferek, R. J.: 2000, *Journal of Atmospheric Sciences* **57**, 2684

Allen, R. J. and Landuyt, W.: 2014, *Journal of Geophysical Research: Atmospheres* **119(8)**, 4808

Allen, R. J. and Sherwood, S. C.: 2010, *Geophys. Res. Lett.* **37**, L07702

Amiri-Farahani, A., Allen, R. J., Neubauer, D., and Lohmann, U.: 2017, *Atmospheric Chemistry and Physics* **17(10)**, 6305

Anderson, J., Balaji, V., Broccoli, A., Cooke, W., Delworth, T., Dixon, K., Donner, L., Dunne, K., Freidenreich, S., Garner, S., Gudgel, R., Gordon, C., Held, I., Hemler, R., Horowitz, L., Klein, S., Knutson, T., Kushner, P., Langenhost, A., Lau, N., Liang, Z., Malyshev, S., Milly, P., Nath, M., Ploshay, J., Ramaswamy, V., Schwarzkopf, M., Shevliakova, E., Sirutis, J., Soden, B., Stern, W., Thompson, L., Wilson, R., Wittenberg, A., Wyman, B., and GFDL Global Atmospheric Model Dev: 2004, *J. Climate* **17**, 4641

Ban-Weiss, G. A., Cao, L., Bala, G., and Caldeira, K.: 2012, *Climate Dyn.* **38**, 897

Bond, T. C., Doherty, S. J., Hahey, D. W., and et al.: 2013, *J. Geophys. Res.* **118**, 5380

Boucher, O., Randall, D., Artaxo, P., Bretherton, C., Feingold, G., Forster, P., Kerminen, V.-M., Kondo, Y., Liao, H., Lohmann, U., Rasch, P., Satheesh, S., Sherwood, S., Stevens, B., and Zhang, X.: 2013, *Clouds and Aerosols. In: Climate Change 2013: The Physical Science Basis. Contribution of Working Group I to the Fifth Assessment Report of the Intergovernmental Panel on Climate Change*, Cambridge University Press, Cambridge, United Kingdom and New York, NY, USA

Brenguier, J.-L., Pawlowska, H., Schüller, L., Preusker, R., Fischer, J., and Fouquart, Y.: 2000, *Journal of Atmospheric Sciences* **57**, 803

Brioude, J., Cooper, O. R., Feingold, G., Trainer, M., Freitas, S. R., Kowal, D., Ayers, J. K., Prins, E., Minnis, P., McKeen, S. A., Frost, G. J., and Hsie, E.-Y.: 2009, *Atmospheric Chemistry & Physics* **9(22)**, 8841

Chen, T., Rossow, W. T., and Zhang, Y. C.: 2000, *J. Climate* **13**, 264

Chen, Y.-C., Christensen, M. W., Stephens, G. L., and Seinfeld, J. H.: 2014, *Nature Geosc* **7(D5)**, 643

Chung, C. E.: 2006, *J. Korean. Meteor. Soc.* **42(6)**, 411

Chung, C. E., Chu, J.-E., Lee, Y., van Noije, T., Jeoung, H., Ha, K.-J., and Marks, M.: 2016, *Atmospheric Chemistry and Physics* **16(13)**, 8071

Chung, C. E., Ramanathan, V., and Decremer, D.: 2012, *Proc. Natl. Acad. Sci.* **109(29)**, 11624

Chung, C. E., Ramanathan, V., Kim, D., and Podgorny, I. A.: 2005, *J. Geophys. Res.* **110**, D24207, doi:10.1029/2005JD006356

Cohen, J. B. and Wang, C.: 2014, *Journal of Geophysical Research: Atmospheres* **119(1)**, 307

Doherty, O. M. and Evan, A. T.: 2014, *Geophys. Res. Lett.* **41**, 6935

Evan, A. T., Dunion, J., Foley, J. A., Heidinger, A. K., and Velden, C. S.: 2006, *Geophys. Res. Lett.* 33

Evan, A. T., Foltz, G. R., Zhang, D., and Vimont, D. J.: 2011, *Nature Geoscience* **4**, 762

Garrett, T. J., Zhao, C., and Novelli, P. C.: 2010, *Tellus B* **62(3)**, 190

Gettelman, A., Liu, X., Ghan, S. J., Morrison, H., Park, S., Conley, A. J., Klein, S. A., Boyle, J., Mitchell, D. L., and Li, J. L. F.: 2010, *J. Geophys. Res* **115**, D18216, doi:10.1029/2009JD013797

Ghan, S. J.: 2013, *Atmos. Chem. Phys.* **13**, 9971

Goudie and Middleton: 2001, *Earth-Science Reviews* **56**, 179

Gryspeerdt, E., Quaas, J., and Bellouin, N.: 2016, *Journal of Geophysical Research (Atmospheres)* **121**, 3566

Hack, J.: 1994, *J. Geophys. Res.* **99**, 5551

Hansen, J., Sato, M., and Ruedy, R.: 1997, *J. Geophys. Res.* **102**, 6831

Hartmann, D. L., Ockert-Bell, M. E., and Michelsen, M. L.: 1992, *Journal of Climate* **5**, 1281

Hodnebrog, Ø., Myhre, G., and Samset, B. H.: 2014, *Nature Communications* **5**, 5065, http://dx.doi.org/10.1038/ncomms6065

Huang, J., Minnis, P., Lin, B., Wang, T., Yi, Y., Hu, Y., Sun-Mack, S., and Ayers, K.: 2006, *Geophysical Research Letters* **33(6)**, n/a, L06824

Huang, J., Wang, T., Wang, W., Li, Z., and Yan, H.: 2014, *Journal of Geophysical Research*

(Atmospheres) 119

Hui, W., Cook, B., Rvai, S., and Fuentes, J. D.: 2008, *Water Resour Res* 44, W05202

Huneeus, N., Schulz, M., Balkanski, Y., Griesfeller, J., Prospero, J., Kinne, S., Bauer, S., Boucher, O., Chin, M., Dentener, F., Diehl, T., Easter, R., Fillmore, D., Ghan, S., Ginoux, P., Grini, A., Horowitz, L., Koch, D., Krol, M. C., Landing, W., Liu, X., Mahowald, N., Miller, R., Morcrette, J.-J., Myhre, G., Penner, J., Perlwitz, J., Stier, P., Takemura, T., and Zender, C. S.: 2011, *Atmospheric Chemistry and Physics* **11(15)**, 7781

Johnson, B. T., Shine, K. P., and Forster, P. M.: 2004, *Quarterly Journal of the Royal Meteorological Society* **130**, 1407

Kaufman, Y. J., Boucher, O., Tanré, D., Chin, M., Remer, L. A., and Takemura, T.: 2005, *Geophys. Res. Lett.* 9(32)

Kishcha, P., da Silva, A., Starobinets, B., Long, C., Kalashnikova, O., and Alpert, P.: 2015, *International Journal of Remote Sensing* **13(6)**, 3423

Koch, D. and Del Genio, A. D.: 2010, *Atmospheric Chemistry & Physics* **10(16)**, 7685

Koch, D., Schulz, M., Kinne, S., McNaughton, C., Spackman, J. R., Balkanski, Y., Bauer, S., Berntsen, T., Bond, T. C., Boucher, O., Chin, M., Clarke, A., De Luca, N., Dentener, F., Diehl, T., Dubovik, O., Easter, R., Fahey, D. W., Feichter, J., Fillmore, D., Freitag, S., Ghan, S., Ginoux, P., Gong, S., Horowitz, L., Iversen, T., A., K., Klimont, Z., Kondo, Y., Krol, M., Liu, X., Miller, R., Montanaro, V., Moteki, N., Myhre, G., Penner, J. E., Perlwitz, J., Pitari, G., Reddy, S., Sahu, L., Sakamoto, H., Schuster, G., Schwarz, J. P., Seland, Ø., Stier, P., Takegawa, N., Takemura, T., Textor, C., van Aardenne, J. A., and Zhao, Y.: 2009, *Atmos. Chem. Phys.* **9(22)**, 9001

Koffi, B., Schulz, M., Bréon, F.-M., Dentener, F., Steensen, B. M., Griesfeller, J., Winker, D., Balkanski, Y., Bauer, S. E., Bellouin, N., Berntsen, T., Bian, H., Chin, M., Diehl, T., Easter, R., Ghan, S., Hauglustaine, D. A., Iversen, T., Kirkevåg, A., Liu, X., Lohmann, U., Myhre, G., Rasch, P., Seland, Ø., Skeie, R. B., Steenrod, S. D., Stier, P., Tackett, J., Takemura, T., Tsigaridis, K., Vuolo, M. R., Yoon, J., and Zhang, K.: 2016, *Journal of Geophysical Research: Atmospheres* **121(12)**, 7254

Kok, J. F., Ridley, D. A., Zhou, Q., Miller, R. L., Zhao, C., Heald, C. L., Ward, D. S., Albani, S., and Haustein, K.: 2017, *Nature Geosci* **10**, 274

Koren, I., Kaufman, Y. J., Remer, L. A., and Martins, J. V.: 2004, *Science* **303**, 1342

Lee, K. and Chung, C. E.: 2013, *Atmospheric Chemistry and Physics* **13(5)**, 2907

Li, R., Min, Q.-L., and Harrison, L.: 2010, *J. Atmos. Sci* **67**, 805

Liu, J., Fan, S., Horowitz, L. W., and Levy, H.: 2011, *Journal of Geophysical Research: Atmospheres* **116(D4)**, 10.1029/2010JD015145

Liu, J. and Li, Z.: 2014, *Atmospheric Chemistry & Physics* **14**, 471

Liu, Z., Vaughan, M., Winker, D., Kittaka, C., Getzewich, B., Kuehn, R., Omar, A., Powell, K., Trepte, C., and Hostetler, C.: 2009, *Journal of Atmospheric and Oceanic Technology* **26(7)**, 1198

Mahajan, S., Evans, K. J., Hack, J. J., and Truesdale, J. E.: 2013, *Journal of Climate* **26(20)**, 8223

Mahowald, N. and Kiehl, L.: 2003, *Geophys. Res. Lett.* **30**, 28

McComiskey, A., Feingold, G., Frisch, A. S., Turner, D. D., Miller, M. A., Chiu, J. C., Min, Q., and Ogren, J. A.: 2009, *Journal of Geophysical Research (Atmospheres)* **114**, D09203

Medeiros, B. and Stevens, B.: 2011, *Climate Dynamics* **36**, 385

Ming, Y., Ramaswamy, V., and Persad, G.: 2010, *Geophys. Res. Lett.* **37**, L13701, doi: 10.1029/2010GL042895

Moorthi, S. and Suarez, M. J.: 1992, *Mon. Wea. Rev.* **120**, 978

Morrison, H. and Gettelman, A.: 2008, *J. Climate* **21**, 3642

Myhre, G., Forster, P. M., Samset, B. H., Hodnebrog, Ø., Sillmann, J., Aalbergsjø, S. G., Andrews, T., Boucher, O., Faluvegi, G., Fläschner, D., Iversen, T., Kasoar, M., Kharin, V., Kirkevåg, A., Lamarque, J.-F., Olivié, D., Richardson, T. B., Shindell, D., Shine, K. P., Stjern, C. W., Takemura, T., Voulgarakis, A., and Zwiers, F.: 2017, *Bulletin of the American Meteorological Society* **98(6)**, 1185

Myhre, G. and Samset, B. H.: 2015, *Atmospheric Chemistry and Physics* **15(5)**, 2883

Myhre, G., Shindell, D., Bréon, F.-M., Collins, W., Fuglestvedt, J., Huang, J., Koch, D., Lamarque, J.-F., Lee, D., Mendoza, B., Nakajima, T., Robock, A., Stephens, G., Takemura, T., and Zhang, H.: 2013, *Anthropogenic and Natural Radiative Forcing. In: Climate Change 2013: The Physical Science Basis. Contribution of Working Group I to the Fifth Assessment Report of the Intergovernmental Panel on Climate Change [Stocker, T.F., D. Qin, G.-K. Plattner, M. Tignor, S.K. Allen, J. Boschung, A. Nauels, Y. Xia, V. Bex and P.M. Midgley (eds.)]*, Technical report, Cambridge University Press, Cambridge, United Kingdom and New York, NY, USA

Neale, R. B., Gettelman, A., Park, S., and et al.: 2010a, *Description of the NCAR Community Atmosphere Model (CAM 5.0)*, Technical Report NCAR/TN-486+STR, National Center for Atmospheric Research, Boulder, CO, 268 pp.

Neale, R. B., Richter, J. H., Conley, A. J., Park, S., Lauritzen, P. H., Gettelman, A., Williamson, D. L., Rasch, P. J., Vavrus, S. J., Taylor, M. A., Collins, W. D., Zhang, M., and Lin, S.-J.: 2010b, *Description of the NCAR Community Atmosphere Model (CAM 4.0)*, Technical Report NCAR/TN+STR, National Center for Atmospheric Research, Boulder, CO, 194 pp.

Park, S. and Allen, R. J.: 2015, *Geophysical Research Letters* **42(23)**, 10,438

Park, S. and Bretherton, C. S.: 2009, *J. Climate* **22**, 3449

Perlwitz, J. and Miller, R. L.: 2010, *J. Geophys. Res.* **115**, D08203, doi:10.1029/2009JD012637

Prospero, J. M.: 1999, *Proceedings of the National Academy of Sciences of the United States of America* **96(7)**, 3396

Quaas, J., Boucher, O., Bellouin, N., and Kinne, S.: 2008, *Journal of Geophysical Research: Atmospheres* **113(D5)**, n/a, D05204

Quaas, J., Boucher, O., and Lohmann, U.: 2006, *Atmospheric Chemistry & Physics* **6**, 947

Ramanathan, V. and Carmichael, G.: 2008, *Nature Geosci.* **1**, 221

Randall, D. A., Rossow, W. T., and Zhang, Y. C.: 1984, *Tellus* **36A**, 446

Randles, C. A., Colarco, P. R., and Silva, A.: 2013, *Journal of Geophysical Research: Atmospheres* **118(1)**, 149

Rasch, P. J. and Kristjánsson, J. E.: 1998, *J. Climate* **11**, 1587

Remer, L. A., Kaufman, Y. J., Tanré, D., Mattoo, S., Chu, D. A., Martins, J. V., Li, R.-R., Ichoku, C., Levy, R. C., Kleidman, R. G., Eck, T. F., Vermote, E., and Holben, B. N.: 2005, *Journal of Atmospheric Sciences* **62**, 947

Rosenfeld, D., Chemke, R., Prather, K., Suski, K., Comstock, J. M., Schmid, B., Tomlinson, J., and Jonsson, H.: 2014, *Atmospheric Research* **135**, 112

Rosenfeld, D., Rudich, Y., and Lahav, R.: 2001, *Proceedings of the National Academy of Science* **98**, 5975

Rotstayn, L. D.: 1997, *Q. J. R. Meteorol. Soc.* **123**, 1227

Rotstayn, L. D., Ryan, B. F., and Katzfey, J. J.: 2000, *Mon. Wea. Rev.* **128**, 1070

Samset, B. H. and Myhre, G.: 2015, *Journal of Geophysical Research: Atmospheres* **120(7)**, 2913

Samset, B. H., Myhre, G., Forster, P. M., Hodnebrog, Ø., Andrews, T., Faluvegi, G., Fläschner, D., Kasoar, M., Kharin, V., Kirkevåg, A., Lamarque, J.-F., Olivié, D., Richardson, T., Shindell, D., Shine, K. P., Takemura, T., and Voulgarakis, A.: 2016, *Geophysical Research Letters* **43(6)**, 2782

Sand, M., Iversen, T., Bohlinger, P., Kirkevåg, A., Seierstad, I., Seland, Ø., and Sorteberg, A.: 2015, *Journal of Climate* **28(6)**, 2512

Schwarz, J. P., Spackman, J. R., Gao, R. S., Watts, L. A., Stier, P., Schulz, M., Davis, S. M., Wofsy, S. C., and Fahey, D. W.: 2010, *Geophys. Res. Lett.* **37**, L18812, doi:10.1029/2010GL044372

Slingo, A.: 1990, *nature* **343**, 49

Stephens, G. L. and Greenwald, T. J.: 1991, *Journal of Geophysical Research (Atmospheres)* **96**, 15325

Stier, P.: 2016, *Atmospheric Chemistry & Physics* **16(10)**, 6595

Stjern, C. W., Samset, B. H., Myhre, G., Forster, P. M., Hodnebrog, Ø., Andrews, T., Boucher, O., Faluvegi, G., Iversen, T., Kasoar, M., Kharin, V., Kirkevåg, A., Lamarque, J.-F., Olivié, D., Richardson, T., Shawki, D., Shindell, D., Smith, C. J., Takemura, T., and Voulgarakis, A.: 2017, *Journal of Geophysical Research: Atmospheres* **122(21)**, 11,462

Tiedtke, M.: 1993, *Mon. Wea. Rev.* **121**, 3040

Tsamalis, C., Chédin, A., Pelon, J., and Capelle, V.: 2013, *Atmospheric Chemistry & Physics* **13(22)**, 11235

Wang, W., Huang, J., Minnis, P., Hu, Y., Li, J., Huang, Z., Ayers, J. K., and Wang, T.: 2010, *Journal of Geophysical Research: Atmospheres* **115(D4)**, n/a, D00H35

Wilcox, E. M.: 2010, *Atmospheric Chemistry & Physics* **10(23)**, 11769

Winker, D. M., Tackett, J. L., Getzewich, B. J., Liu, Z., Vaughan, M. A., and Rogers, R. R.: 2013, *Atmospheric Chemistry and Physics* **13(6)**, 3345

Zarzycki, C. M. and Bond, T. C.: 2010, *Geophysical Research Letters* **37(20)**, 10.1029/2010GL044555

Zhang, G. J. and McFarlane, N. A.: 1995, *Atmosphere-Ocean* **33**, 407